University of Nevada, Reno

Transient water flow around a buried artificial landmine and the associated surface thermal response.

A thesis submitted in partial fulfillment of the requirements for the degree of Master of Science in Hydrogeology

by

Walker Blackburn Weir

Dr. Mark B. Hausner / Thesis Advisor
Dr. Eric McDonald / Thesis Advisor

August, 2020

THE GRADUATE SCHOOL

We recommend that the thesis
prepared under our supervision by

entitled

be accepted in partial fulfillment of the
requirements for the degree of

Advisor

Co-advisor

Graduate School Representative

David W. Zeh, Ph.D., Dean
Graduate School

Abstract

The detection of landmines via surface thermal sensing may be improved by applying soil modeling to the problem. Increased water retention above a buried, impermeable object changes the flow of water and heat thereby altering the surface expression of heat. To explore this idea, experiments at the Desert Research Institute's Ecologically Controlled Enclosed Lysimeter Laboratories (EcoCELL) were used to measure transient heat and water distribution around buried artificial landmines. A series of Hydrus 1D and 2D models are presented, that simulate the EcoCELL laboratory experiments and constrain the soil properties of the tested soil. Hydrus 1D models simulating endmember soil conditions supplemented the 2D modeling by adding a surface energy balance. Results indicate a potential for soil watering to enhance the surface thermal signature of a buried object. The 2D modeling show a clear difference in water and heat flow dynamics above a target versus adjacent to the target. The 1D modeling indicates that soil watering has a stronger effect than the thermal properties of the target on surface temperature signals. Limitations of the Hydrus modeling software are discussed, and recommendations for future modeling efforts are detailed.

For Courtney, my love.

iii

Acknowledgments

Acronyms and Variables

Acronyms:

VWC – volumetric water content

SWR – short-wave radiation

LWR – long-wave radiation

VPD – vapor pressure deficit

SWRC – soil water retention curve

YPG – Yuma Proving Grounds

VGM – Van Genuchten-Mualem

UBC – Upper Boundary Condition

LBC – Lower Boundary Condition

Variables:

Φ – local heat flux density

λ – thermal conductivity

$\lambda(\theta)$ – apparent thermal conductivity

T – temperature

C_v – volumetric heat capacity

κ – thermal diffusivity

j – energy (joules)

ε – emissivity

σ – Stephan-Boltzmann constant

Q – energy of latent heat exchange

m – mass

L – latent heat of phase change

P – fluid pressure

ρ – density

g – gravitational acceleration

z – elevation

V – fluid velocity

ψ_m – matric potential

θ – volumetric water content

θ_r – residual water content

θ_s – saturated water content

h_c – height of capillary rise

γ – surface tension

φ – wetting contact angle

r – pore radius

q – hydraulic flux

K_s – saturated hydraulic conductivity

D_{10} – 10th percentile grain diameter

μ – viscosity

w – weight of permeant

S_0 – surface area per volume of particles

e – porosity

h – pressure head

h_a – air entry pressure

H – hydraulic head

α – inverse air entry pressure

$C(\theta)$ – volumetric heat capacity of soil

C_w – volumetric heat capacity of water

t – time

β_t – thermal dispersivity

ε_r – relative permittivity

Contents

List of Tables

List of Figures

Introduction

This work is motivated by the problems surrounding landmine detection, with the aim of demonstrating the role of soil physics on the thermal expression of a landmine at the ground surface. The Landmine and Cluster Munition Monitor reported 8,605 landmine casualties in 2016 (78% of which were civilian), and over 110,000 casualties since 1999 (Landmine Monitor 2016). The variety of materials, dimensions, and depths of buried landmines make their detection particularly challenging, not to mention dangerous. Numerous detection methods exist to identify landmines including chemical sniffers, subsurface imaging technologies (such as ground penetrating radar, metal detectors, and acoustic sensors), and sensors that detect thermal anomalies at the soil surface (van Dam 2005, Donskoy 2002).

Thermal sensing provides a remotely deployable, non-contact means of detecting buried objects, and allows for scans of larger areas than other methods (van Dam 2005). The thermal and hydraulic properties of landmines are usually different from the surrounding soil, and from other natural objects such as rocks or organics (Smits 2013). This contrast may cause measurable thermal variations between the soil above and adjacent to a buried landmine (Bruschini 1997). For thermal sensing to be effective as a means to detect landmines, it is necessary to know the volumetric heat capacity, thermal conductivity, texture, and moisture content of the soil (Das 2001, van Dam 2005, Smits 2013). It is also important to understand how surface temperature signals respond to natural environmental variability.

This research is meant to further understanding of heat and fluid dynamics in the soil surrounding impermeable near-surface objects such as landmines. This study explores the primary controls on surface temperature above buried objects during dry conditions and across a range of soil moisture contents. Laboratory and digital models are presented to both demonstrate the change in surface thermal signature associated with water ponded above a buried object, and to examine the effects of a target's thermal properties on the surrounding soil under a range of moisture conditions.

Background

The soil zone (also called the vadose zone or unsaturated zone) is the uppermost layer of the earth surface, which can support the growth of plants (Fetter 2001). Soil is composed of mineral, water, gas, and organic material fractions (DeVries 1963). Each constituent has varied physical properties and inhomogeneous distributions, so soil is often approximated as a unified whole (in bulk). Measuring the bulk properties of a volume of soil allows the combined effects of all parts of the soil to be considered and unified. Soil has an inherent porosity, the proportion of void space to total volume (Dingman 2015). The saturated water content of a soil (θ_s) is equal to porosity. Water contents can vary widely over horizontal and vertical distances less than 1 meter (van Dam 2005). This study examines approximately the 10 to 200 cm scale.

Heat Transport Mechanisms

Modeling heat and water flow in soil requires understanding the physical mechanics that govern flow through the system. The primary mechanisms of heat transport are latent heat of phase changes, radiation, conduction, and convection (Carslaw & Jaeger 1959). For

this review, advection of heat is examined instead of convection since bulk fluid flow is a common form of motion-driven heat transfer in soil. For heat flow, the process of advection is driven by motion of water, while convection is driven by thermal gradients (Fetter 2001, Carslaw & Jaeger 1959). Radiation is the transfer of energy as electromagnetic waves (Carslaw & Jaeger 1959). Conduction is the physical transfer of energy from molecular collisions (Carslaw & Jaeger 1959). Heat exchange may also be sensible or latent. Sensible heat exchange (heat you can feel) has an associated temperature gradient (Dingman 2015). Sensible heat flux is a form of conduction, which occurs only between the atmosphere and earth (Dingman 2015). Temperature is simply a measure of the thermal energy of a system, i.e. the concentration of heat. Latent heat is the energy required to change the phase of a substance (e.g., from liquid to vapor) without changing its temperature, though the process of latent heat exchange both depends on and influences the temperature of surrounding media (Dingman 2015). Material properties that influence heat flow dynamics include heat capacity, thermal conductivity, thermal diffusivity, albedo, and emissivity (Furbish 1996). These properties and the mechanisms of their influence are described in more detail below.

Conductive Heat and Thermal Conductivity

The process of heat conduction in soil depends on thermal gradient and bulk thermal conductivity (λ), or the ability of a material to conduct heat, expressed as power per unit area per unit temperature gradient ($W{\cdot}m^{-1}{\cdot}K^{-1}$) (Furbish 1996). Fourier's law quantifies conductive heat flow through a substance, in which the heat flux through a unit area per unit time is equal to thermal conductivity multiplied by the negative temperature gradient (Fourier 1822).

$$\Phi = -\lambda\nabla T \qquad\qquad\qquad \text{Eqn. 1}$$

Where Φ is local heat flux density ($W\cdot m^{-2}$), λ is thermal conductivity ($W\cdot m^{-1}\cdot K^{-1}$), and ∇T is thermal gradient ($K\cdot m^{-1}$).

Conduction occurs through the interaction of molecules, and thus is largely dependent on connections through liquid and solid phases (Schaetzl & Thompson 2015). A dry soil will conduct heat mostly through grain-to-grain contact, so heat conduction will then be controlled by mineral composition and density (Smits 2010). Lower porosity is also associated with higher thermal conductivity, as there is then more conductive mass per unit volume (Smits 2010). Quartz is more common in coarse-textured soils, making coarser soils generally better heat conductors than fine-textured soils (Schaetzl & Thompson 2015). Soil compaction or turbation will also change soil density and the overall grain-to-grain contact area within a soil, thus affecting heat conduction (Caldwell et al. 2012).

Bulk soil thermal conductivity is determined by the combination of the mineral grains plus the water/air medium (DeVries 1963), making grain size distribution and soil moisture determining factors for λ (Smits 2010). Bulk thermal conductivity is sensitive to water content. As soil water content increases and pores fill, conductive surface area will increase and λ will rise. For most soils, this increase is greatest at low water contents, but tapers off as additional water content increases correspond to relatively smaller increases in conductive surface area (Figure 1A). Quartz is abundant in many soils and has a high λ of around 3 $W\cdot m^{-1}\cdot K^{-1}$, while air has a very low λ approximately 300 times less than quartz (Schaetzl & Thompson 2015). The λ of water lies between that of rock and air, around 0.6 $W\cdot m^{-1}\cdot K^{-1}$ (Furbish 1996). Thermal conductivity for water and air both increase with higher

temperature, over the natural range of soil temperatures (Engineeringtoolbox.com, 2019). While thermal conductivity has a temperature dependence for some materials, it is frequently assumed to be negligible (Carslaw and Jaeger 1959, Van Wijk 1963).
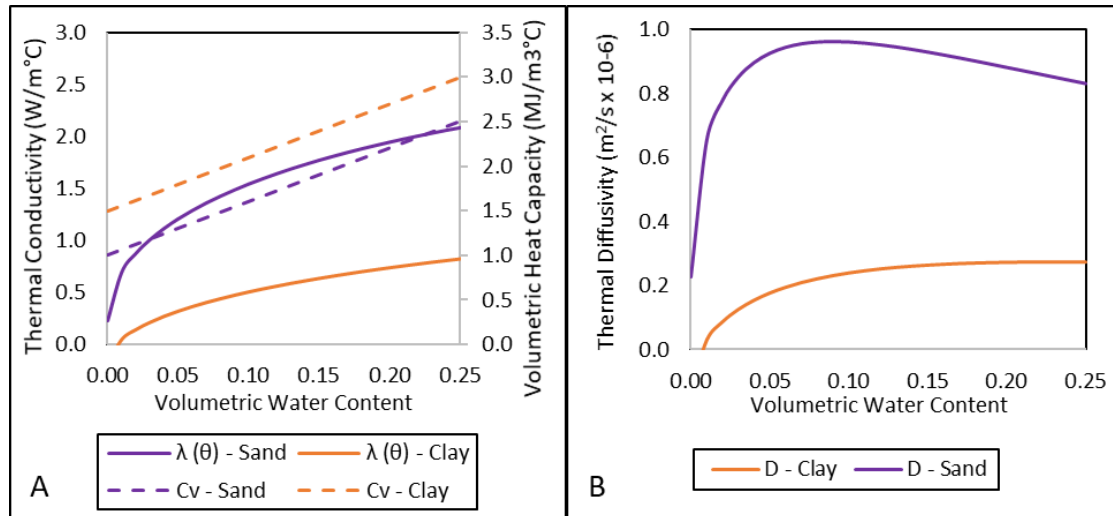
Figure 1: Generic profiles of thermal conductivity ($\lambda(\theta)$), volumetric heat capacity (CV), and thermal diffusivity (D) for a sand and a clay, over 0 to 25 percent volumetric water content. Thermal conductivities are from Chung and Horton (1985) parameters. Volumetric heat capacities are estimates from values reported by Abu-Hamdeh (2003). Thermal diffusivity is calculated as thermal conductivity divided by volumetric heat capacity (here denoted D rather than κ)

Specific Heat, Heat Capacity, Volumetric Heat Capacity

The specific heat ($J \cdot kg^{-1} \cdot K^{-1}$) of a material is the amount of energy required to change the temperature of one kilogram by one kelvin (Furbish 1996). Heat capacity ($J \cdot K^{-1}$) is a related property, which is specific heat multiplied by the mass of a discrete volume of material. Soil is generally a matrix of solids containing liquid and gas in pore spaces, so the bulk volumetric heat capacity (C_V) is a function of water content. Volumetric heat capacity is specific heat multiplied by material density, making it a measure per volume

rather than per mass. As pores are saturated with water, the bulk C_V of a given soil volume will increase since water has a higher C_V (4.182 $MJ \cdot m^{-3} \cdot K^{-1}$) than air (approximately 1225 $J \cdot m^{-3} \cdot K^{-1}$) or the mineral component of soils (Elger 2009). The increase in bulk C_V with increasing water content is linear (Figure 1A). Temperature dependencies for specific heat are often considered negligible in comparison to changes to bulk soil heat capacity from changes in water content (Van Wijk 1963).

Thermal Diffusivity

Thermal diffusivity (κ) is the ratio of thermal conductivity to volumetric heat capacity and represents the rate at which temperature changes propagate through a material (Carslaw & Jaeger 1959). Dry soil has lower thermal diffusivity than wet soil, so dry soil propagates temperature changes more slowly than wet soil (Van Wijk 1963). Some metals such as aluminum and lead have very high values of κ and will change temperature more rapidly than quartz (Smits 2013). Thermal conductivity and thermal diffusivity both vary more from 0-15% VWC than from 15-35%, with 0-15% VWC being more typical of surface soils (van Dam 2005).

Unlike thermal conductivity, thermal diffusivity does not change monotonically with increasing moisture content (Figure 1B). While volumetric heat capacity increases linearly with increasing water content, the change in thermal conductivity is nonlinear. For a completely dry soil, thermal conduction occurs almost entirely through grain-to-grain contacts with negligible conduction through air (Schaetzl & Thompson 2015). As pores begin to fill with water, water is held on grains as thin films (Schaetzl & Thompson 2015). This adds to the effective surface area through which heat can be conducted, causing a rapid rise in thermal conductivity. As pores continue to wet up, the relative increase in

thermal conductivity tapers off (Schaetzl & Thompson 2015). Concurrently, the high specific heat of water raises the volumetric heat capacity of the soil linearly. With increasing VWC, the linear increase in C_V and nonlinear increase in $\lambda(\theta)$ creates an inflection point for thermal diffusivity for many soils (Figure 1B). When the relative increase in soil C_V outpaces the increase in soil λ, the bulk thermal diffusivity of the soil will decrease.

<div align="center">Radiative Heat</div>

Short-wave radiation (SWR) is energy emitted by the sun, with most energy in the visible light spectrum (0.4 - 0.7 μm wavelength) and near infrared (<4 μm; Dingman 2015). Under most natural conditions, SWR is the primary heat source in soils (Dingman 2015). Some SWR is absorbed or reflected by the atmosphere, and may then be re-radiated or scattered toward the Earth (Dingman 2015). A portion of incident radiation at the ground surface is reflected upon contact with the ground surface depending on the albedo of the soil (Dingman 2015). Albedo is the proportion of diffuse reflection of direct solar radiation in the visible spectrum (Dingman 2015). Albedo depends on the color or reflectivity of a surface, which may be altered by latitude (sun angle), surface slope, and surface roughness (Dingman 2015). Reflectivity is an optical property, simply meaning the proportion of incident light that will be reflected by a surface based on wavelength, angle, and the material (Dingman 2015). Ground surface albedo can range from as low as 0.06 (94% absorption) for open ocean to as high as 0.9 (only 10% absorption) for white, fresh snow (Van Wijk 1963). Light-colored soils may have high albedo, though this is reduced by water, which very effectively absorbs radiative energy (Van Wijk 1963). Non-reflected SWR heats the soil while the sun is shining, and the energy is then transported, stored, or

used as latent heat (Dingman 2015). Energy from solar heating will be held by the ground or atmosphere, transmitted into the ground, re-radiated out as long-wave radiation (LWR) (4-50 μm), or expended as latent or sensible heat flux (Van Wijk 1963).

All materials emit longwave radiation depending on their temperature and emissivity (Eqn. 2), including re-radiated LWR toward the ground from sources such as vegetation and clouds. To account for this balance, net radiation measured at the ground surface (incoming minus outgoing SWR and LWR) is often used to estimate surface energy flux. The amount of energy radiated from a body can be described by the Stefan-Boltzmann law (Boltzmann 1884).

$$j = \varepsilon \sigma T^4$$ Eqn. 2

Where j is energy radiated per unit area per unit time (kg·m^2·s^{-2}), ε is emissivity (<1), σ is the Stefan-Boltzmann constant (W·m^{-2}·K^{-4}), and T is temperature (K).

Emissivity, ε, is the effectiveness of a body to radiate thermal energy compared to a perfectly efficient energy emitter (DeVries 1963). Water has a high emissivity of 0.95 and is a good emitter of long-wave radiation (Dingman, 2015). Soil emissivity is also typically close to 1 and is generally higher for saturated soil. McDonald et al. (2015) found that emissivity increased with increasing saturation for the six soil samples they tested. Soil emissivity depends largely on surface texture. A smooth surface will emit energy less effectively than a rough surface at natural temperatures (Shati et al. 2011). As described by the Stefan-Boltzmann law, the amount of radiated energy off a surface has a strong dependence on the surface temperature (Eqn. 2).

Latent Heat

Latent energy exchange occurs with the phase change of a material. Water evaporation consumes energy and thus the process will cool the surrounding media as energy is used for phase change (Dingman 2015). To drive evaporation, a system must have water present to evaporate, available energy to drive the heat transfer, a vapor pressure deficit (VPD) governed by the relative humidity of the atmosphere, and usually stimulation to the system such as wind (Dingman 2015). The VPD is the difference between the partial pressure of water vapor in the air and the potential vapor pressure for fully saturated (i.e., 100% relative humidity) air. Saturated vapor pressure increases with temperature, so there is a higher potential for evaporation on a hot dry day and a lower potential if the air is close to saturation (Dingman 2015). Latent heat is related to energy by the following equation (Joule 1884):

$$Q = mL \hspace{4cm} \text{Eqn. 3}$$

Where Q is the energy released or absorbed during phase change (kJ), m is mass of material (kg), L is the latent heat of the specific material phase change (i.e. vaporization, melting, etc.) (kJ·kg^{-1}).

The latent heat of vaporization of water, 2.26 x10^6 J·kg^{-1}, is the energy required to change the phase of one kilogram of liquid water to water vapor (Furbish 1997). Various methods exist to measure actual evaporation from a surface (often measured from a pan) or to estimate the potential for evaporation based on environmental conditions. Most potential evaporation estimates account for air temperature or net radiation, while more complex methods include factors such as relative humidity, wind speed, and ground heat flux (Karlsson 2013). Measurement of actual evaporation is difficult, even when using

evaporation pans, since there is usually a bias from pan placement or the scale of measurements. When atmospheric drivers are the limiting factor in determining evaporation potential, but there is plenty of water available for evaporation, estimates of potential evaporation may be closer to actual evaporation, but the timing of water storage near the ground surface must also be considered.

Sensible Heat

Sensible heat flux is a convective, non-radiative form of energy transfer driven by temperature gradients (Dingman 2015). For a surface energy balance, the sensible heat flux considered is between the soil surface and the atmosphere. Surface sensible heat flux depends on air and soil temperature gradients and on wind speed. Energy expended for latent heat exchange does not change the temperature of the material changing phase (water) but does affect the temperature of the surrounding medium (soil) (Dingman 2015). Sensible heat both depends on and alters the temperature of the soil.

Advective Heat

Advection is the transport of heat by the flow of heat-bearing fluid (Fetter 2001). While solar energy is the primary source of radiative energy, the input of water can be a strong source or sink of heat advected into soil. Both radiation and advection alter thermal gradients in soils, thereby influencing conductive heat flux (Carslaw & Jaeger 1959). Advection may bring cooler water into a warm soil or vice versa, depending on the water source and the antecedent soil temperature (Dingman 2015). The extent and rate at which water flows in soils is, like heat, controlled by soil properties and energetic gradients or potentials (Dingman 2015).

Water Flow

Water that condenses out of clouds and falls as precipitation onto the ground surface has a finite number of potential pathways. At the surface water may infiltrate, pond, evaporate, or run off. As water infiltrates into the soil it can fill pore space, move through the soil medium, reach the water table as recharge, or resurface as return flow or evaporated vapor (Fetter 2001). Similar to heat, water flows in soil from higher potential to lower potential, according to the combination of driving potentials from elevation, fluid pressure, and fluid velocity. For fluid energy to be conserved, these energy potentials balance one another, as expressed by the Bernoulli equation. The head form of the Bernoulli equation is as follows (Elger et al. 2009):

$$\frac{P}{\rho g} + z + \frac{V^2}{2g} = constant \qquad \text{Eqn.}$$

4

Where P is fluid pressure (N·m^{-2}), ρ is fluid density (kg·m^{-3}), z is elevation (m), V is fluid velocity (m·s^{-1}), and g is gravitational acceleration (m·s^{-2}). The right side of the equation is constant in the absence of energy input or loss, meaning the above equation is written for steady-state flow (Elger et al. 2009). Note that flow velocities through soil are typically small, on the order of millimeters per second at the high end (Fetter 2001). With velocity raised to the second power, the third (kinematic) term of Equation 4 is negligible for most soil conditions. Total hydraulic head can be broken down into the same three components: elevation head, fluid pressure head, and velocity head. When calculating head potential for soil water flow, fluid velocity is generally ignored (Fetter 2001).

Darcy's law describes the rate of flow of water through saturated porous media as a function of hydraulic conductivity and head gradient (Darcy 1856).

$$q = K_s \frac{dh}{dz} \qquad \text{Eqn. 5}$$

Where q is vertical hydraulic flux ($m \cdot s^{-1}$), K_s is saturated hydraulic conductivity ($m \cdot s^{-1}$), and dh/dz is the head gradient with depth. Saturated hydraulic conductivity (K_s) describes how easily water flows through a saturated porous medium, and depends both on the intrinsic permeability of the medium and on the viscosity and density of the fluid (Law 2004). Using Darcy's law, one can estimate the saturated conductivity of a porous medium by measuring the flux and changes in head.

Water Flow in Unsaturated Soil

To understand unsaturated flow through soil one must consider how the water is transmitted and stored. The water table surface is the point at which pressure head is equal to atmospheric pressure (Dingman 2015). This point has pressure often called zero-gauge, which is absolute pressure referenced to atmospheric pressure. Below the water table soil is fully saturated and fluid pressure is positive. Above the water table fluid flow is still gradient driven, but fluid pressure becomes negative and hydraulic conductivity becomes dependent on soil water content.

Water – H_2O – is a relatively strong polar molecule, meaning it has the potential to adhere to charged soil grains or cohere to other water molecules (Schaetzl & Thompson 2015). Interstitial bonding of water molecules to the soil matrix combined with surface tension of water by cohesive bonds together hold water in soil (Schaetzl & Thompson 2015). The force that holds water to grains and within pores against the force of gravity is a pressure head called the matric potential (ψ_m), sometimes referred to as tension head or

capillary pressure (Radcliffe & Šimůnek 2010). Clays often have polarized faces that readily bond to water, so a clayey soil better retains water than a quartz sand (Schaetzl & Thompson 2015). Matric potential, expressed in units of length, represents the tension or suction a soil exerts on water, and can be thought of as *negative* pressure head. In the same way that water in saturated media flows in response to head gradients, water in unsaturated soils flows in response to gradients in matric potential. Matric potential at and below the water table is zero, as there are no free surfaces for capillarity to take effect (Schaetzl & Thompson 2015).

Residual water content (θ_r) is the volumetric water content (θ) retained by a soil after all gravity-driven drainage has occurred and the soil is under high tension. At residual water content soil moisture is held in pores by cohesive forces between the water molecules and soil matrix (Radcliffe 2010). As water content rises slightly there may be flow through capillarity, the action of water moving due to surface tension. The amount of capillary rise in an ideal tube or pore is given by Jurin's law (adapted from Jurin 1718):

$$h_c = \frac{2\gamma cos\varphi}{\rho g r} \qquad \text{Eqn. 6}$$

Where h_c is height of capillary rise (m), γ is surface tension (N·m^{-1}), φ is the contact angle between liquid surface and pore wall, ρ is liquid density (kg·m^{-3}), g is gravitational acceleration (m·s^{-2}), and r is tube radius (m). In soil, the contact angle depends on the adhesion between the water molecules and the dry soil surface (Radcliffe 2010). Fine-grained soils have higher density of small pore spaces and higher surface area, and can thus retain water by matric forces more effectively than coarser soils (Schaetzl & Thompson 2015). At low water contents, capillarity is an important control on the pressure response

to changes in water content. Capillary action not only allows for much of the water retention in soils, but is also one mechanism by which plants transpire (Dingman 2015).

In the unsaturated zone, hydraulic conductivity (K) depends on water content, denoted K(θ), where θ represents volumetric water content with units of $[L^3L^{-3}]$ (Radcliffe 2010). For a typical soil, K(θ) may range several orders of magnitude between the residual water content and full saturation. Saturated hydraulic conductivity is the maximum K(θ). At residual water content, soil water is held as films on grains and K(θ) = 0 (Schaetzl & Thompson 2015). As pore water increases, as with λ, K increases. The nonlinear relationship between water content, hydraulic head (including matric potential), and hydraulic conductivity can be expressed by Richards' equation (Richards 1931):

$$\frac{\partial \theta(h)}{\partial t} = \frac{\partial}{\partial z}\left(K(h)\left(\frac{\partial h}{\partial z}+1\right)\right)+S \qquad \text{Eqn. 7}$$

Where θ is volumetric water content, t is time, z is depth, K is hydraulic conductivity, h is pressure head (or matric potential), and S is a sink term usually reserved for loss via transpiration. The above equation is the one-dimensional, vertical form of Richards' equation for unsaturated flow, though it can also be written in two or three dimensions. Notably, K is a function of pressure head, which can in turn be related to θ by the ratio $\frac{\partial h}{\partial \theta}$. Since both sides of the equation depend on pressure head, Richards' equation for unsaturated flow is non-linear and must be approximated numerically. The "+1" on the right side of the equation represents the vertical unit hydraulic gradient, owing to changing elevation head component of matric potential with changing depth.

Pressure head (matric potential) as a function of volumetric water content $h(\theta)$ is depicted in a soil water retention curve (SWRC) or moisture sorption curve. The SWRC is

a useful function for comparing soils and depends largely on soil physical properties. A typical SWRC has an S-shape with two inflection points – one approaching residual water content and one near saturated water content (Figure 2).
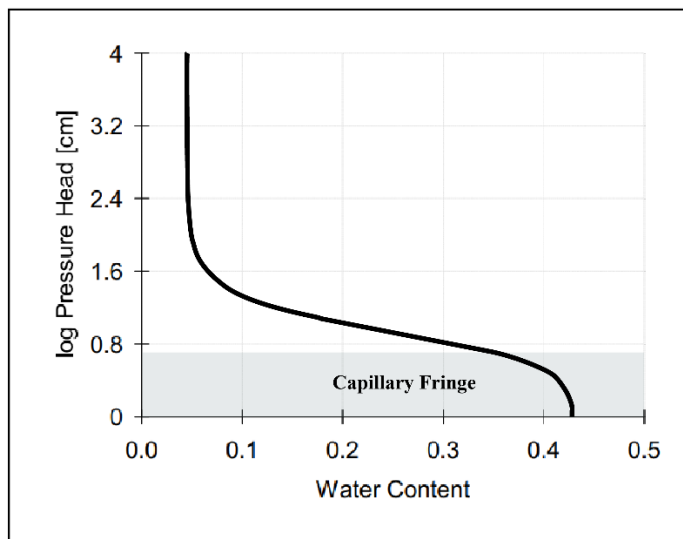
Figure 2: Soil water retention curve for the sand used for this study. The vertical axis is a log scale to exaggerate the inflection points. Though the values of the y-axis are positive, they represent matric head for the unsaturated zone – a negative pressure head. The blue zone at the bottom is the capillary fringe. This figure was modified from Hydrus 2D output.

The capillary fringe is a zone of near-saturation between the water table and vadose zone and is bound by the saturated-end inflection point on a SWRC. Within the capillary fringe, small changes in head or water content can result in large changes in water level and conductivities (Radcliffe & Šimůnek 2010). Air entry pressure (h_a) is a measure of the required negative fluid pressure to overcome fluid surface tension and allow air to comingle in pores. The value of h_a determines the thickness of the capillary fringe and is an important consideration when modeling SWRC. Conversely, at very low water contents a small

change in water content may also result in a large consequent change in head, as indicated by the low-VWC inflection point on a SWRC.

The Van Genuchten-Mualem (VGM) model (Mualem 1976) is used to calculate the SWRC for various soils and is an adaptation of a previous model developed by Brooks and Corey in 1964. The Brooks and Corey model relates water content to hydraulic head as follows (Brooks and Corey 1964):

$$\frac{\theta}{\theta_{sat}} = \frac{1}{h_a} H^{-b} \qquad \text{Eqn. 8}$$

Where θ and θ_{sat} are variable and saturated water content, respectively ($m^3 \cdot m^{-3}$), h_a is air entry pressure (m), H is total hydraulic head (m), and b is a fitting parameter. The VGM model relates the water content terms to residual water content and adds additional fitting parameters (Mualem 1967):

$$\frac{\theta - \theta_r}{\theta_{sat} - \theta_r} = \frac{1}{(1+|\alpha h|^n)^m} \qquad \text{Eqn. 9}$$

Where θ, θ_{sat}, and θ_r are variable, saturated, and residual water content, respectively, α is the inverse of air-entry pressure h_a, n and m are fitting parameters simplified by the assumption that m=1-(1/n). Note that $\theta_{sat} - \theta_r$ represents maximum effective storage capacity. Das et al. (2001) found storage capacity to be a strong determining factor of water distribution in soils. The relationship between VWC and head is again related to the variable unsaturated hydraulic conductivity that is central to the Richards equation. Hydraulic conductivity also changes drastically at very low water contents (Smits 2010).

Heat and water flow interact in several ways. Higher temperature water has reduced density, reduced viscosity, and reduced surface tension, which lowers the influence of matric potential and increases infiltration capacity (Schaetzl & Thompson 2015). She &

Sleep (1998) show that residual water content will generally decrease as soil temperature rises. Heat can provide energy to change the state of water. Similarly, increased water content may provide more available water for evaporation and thus increased latent heat transfer. As previously mentioned, water has a thermal conductivity an order of magnitude greater than that of air, so volumetric bulk thermal conductivity of a soil will increase with increasing water content. Infiltrating water is the largest potential driver of advected heat in shallow soils.

<div align="center">Modeling Heat and Mass Transfer in Soils with Hydrus 2D</div>

Hydrus is a modeling software developed to simulate water, heat, and solute transport through variably saturated porous media (Šimůnek et al. 2006), and is available in both 1-dimensional (HYDRUS-1D) and 2D (HYDRUS-2D) formats. Hydrus 2D simultaneously solves the 2D Richards equation for both saturated and unsaturated water flow and the 2D advection-dispersion equation for heat or solute transport (Eqns.10 & 11). The 2D version can handle many types of boundary conditions in irregular configurations using a finite-element grid to numerically solve the governing transport equations across the model domain (Radcliffe & Šimůnek 2006). Hydrus software has been applied to a multitude of topics from agriculture to contaminant transport to subsurface flows (Šimůnek 2016), and has been used in similar studies to this (Das 2003, van Dam 2003, Šimůnek 2001).

Like all numerical models, Hydrus models require boundary conditions and initial conditions to set a framework for model calculation, and soil parameters to dictate the behavior of heat and water in the system. Hydrus can be run as a forward model or run inversely. A forward run uses known soil parameters to calculate spatial and temporal flow.

An inverse model takes observed data points and iteratively runs to optimize soil parameters to match observations. Both prescribed and optimized soil parameters can be used with the Van Genuchten-Mualem model for soil retention (Eqn. 10). Hydrus includes a catalog of Van Genuchten-Mualem soil parameters, useful for testing a model or when insufficient soil data are available.

For Hydrus 2D, the Richards equation (Eqn. 7) is resolved in its two-dimensional form:

$$\frac{\partial \theta(h)}{\partial t} = \frac{\partial}{\partial x}\left(K_x(h)\left(\frac{\partial h}{\partial x}\right)\right) + \frac{\partial}{\partial z}\left(K_z(h)\left(\frac{\partial h}{\partial z} + 1\right)\right) + S \qquad \text{Eqn. 10}$$

Where θ is volumetric water content, t is time, x is a horizontal dimension, z is depth, K is hydraulic conductivity, h is pressure head, and S is a sink term usually reserved for loss via transpiration. The 2D form of the Richards equation is also non-linear, requiring an iterative solution. Convergence criteria can be adjusted in the software.

Heat transport is resolved in Hydrus 2D by solving the two-dimensional convection-dispersion equation of the form (Sophocleous 1979):

$$C(\theta)\frac{\partial T}{\partial t} = \frac{\partial}{\partial x_i}\left[\lambda_{ij}(\theta)\frac{\partial T}{\partial x_j}\right] - C_w q_i \frac{\partial T}{\partial x_i} \qquad \text{Eqn. 11}$$

Where $\lambda_{ij}(\theta)$ is apparent thermal conductivity ($W \cdot m^{-1} \cdot K^{-1}$), $C(\theta)$ and C_w are volumetric heat capacities of the soil and water, respectively ($J \cdot m^{-3} \cdot K^{-1}$), T is temperature (K), and t is time. The first term of the right-hand side represents conductive heat flow and the second term represents advective heat flow by water. For the above equation, apparent thermal conductivity ($\lambda(\theta)$) is the sum of volumetric thermal conductivity and macrodispersivity, expressed by de Marsily (1986) as:

$$\lambda(\theta) = \lambda_0(\theta) + \beta_t C_w |q| \qquad \text{Eqn. 12}$$

Where β_t is thermal dispersivity [L]. Other variables are defined previously. Thermal dispersivity has units of length and represents the degree to which heat or fluid is distributed within a soil. Variations in flow path lengths and rates of flow through porous media cause differences of heat and fluid flow from a point or along a path (Fetter 2001). These differences can occur through the soil matrix, or even from variations in flow velocity along pore walls versus through the center of pores (Fetter 2001).

Heat and water transport modeling each require user defined boundary and initial conditions for the model domain. The three system-independent boundary types are Dirichlet (Type 1: specified value), Neumann (Type 2: specified flux), and Cauchy (Type 3: combination). A Type 1 boundary has a specified value in the boundary node, while a Type 2 boundary has a fixed flux (Šimůnek 2006). For a Type 3 boundary there is a specified value, but also a given function for flux on each side of that fixed point. A no-flow boundary condition is a special case of a Type 2 boundary where flux is fixed as zero.

Heat flow boundary conditions in Hydrus can be Type 1, or Type 3, which functions as a no-flow boundary unless heat is added by water. The temperature of said water must be specified. For an upper boundary condition (UBC) Hydrus 2D also allows for a time-varying specified value (average daily temperature and amplitude are specified) boundary condition that approximates diurnal ground surface temperature as a sinusoidal function as follows (Kirkham and Powers, 1972):

$$T_0 = \bar{T} + A \cdot sin\left(\frac{2\pi t^*}{t_p} - \frac{7\pi}{12}\right) \qquad \text{Eqn. 13}$$

Where A is amplitude; t_p is one day; $\bar{T}$ is average soil surface temperature; t^* is local time; and $7\pi/12$ is a phase shift factor forcing the peak temperature to occur at 13:00 hours.

Water boundaries may be set as specified flux or head values, an atmospheric boundary with specified water input and specified evaporation, or several drainage boundary types. Drainage options include seepage face (Type 2: specified zero pressure head), free drainage (Type 3: unit gradient, purely gravity driven), and deep drainage (Šimůnek 2006).

Modeling Heat and Mass Transfer in Soils with Hydrus 1D

Hydrus-1D simulates one-dimensional, vertical heat and mass transport in the unsaturated zone, and allows more sophisticated energy boundary conditions than Hydrus-2D. The atmospheric boundary condition for water flow has several degrees of complexity to choose from depending on data availability. Precipitation and bulk evaporation can be directly input as time-variable data. Physical and meteorological conditions including latitude (sun angle), altitude, emissivity, albedo, wind speed, air temperature range, and relative humidity can all be specified to calculate potential evaporation (Šimůnek 2005).

Hydrus 1D includes three models for estimating potential evapotranspiration (PET), which can modify the upper boundary conditions The Hargreaves (1982) formula is temperature based (Hargreaves 1994, Jensen 1997).

$$PET = 0.0023 R_a (T_m + 17.8)\sqrt{TR} \qquad \text{Eqn. 14}$$

Where PET is potential evapotranspiration (mm·day^{-1}), R_a is extraterrestrial radiation (dependent on location and season)(J·m^{-2}·s^{-1}), T_m is mean daily air temperature (°C), and TR is daily air temperature range (°C).

The Penman-Monteith combination equation for estimating PET is accepted as the most reliable method where there is sufficient meteorological data to support it. The Penman-Monteith equation is as follows (Allen et al. 1998):

$$\lambda ET = \frac{\Delta(R_n - G) + \rho_a C_p \frac{(e_s - e_a)}{r_a}}{\Delta + \gamma\left(1 + \frac{r_s}{r_a}\right)}$$ Eqn. 15

Where λET is latent heat flux (W·m^{-2}), R_n is net radiation (W·m^{-2}), G is soil heat flux (W·m^{-2}), (e_s-e_a) represents VPD (Pa), ρ_a is dry air density (kg·m^{-3}), γ is the psychrometric constant (Pa·K^{-1}), and r_a and r_s are aerodynamic and bulk surface resistances, respectively (m·s^{-1}).

The Hydrus 1D "Energy Balance Boundary Condition" option partitions net radiation into radiative, latent, and sensible heat fluxes at the surface. It also has the benefit of outputting surface temperature if used with a Type 3 heat boundary condition, unlike the Hargraves or Penman-Monteith methods. Assuming an absence of advective heat flux or energy storage, the energy balance for the ground surface can be expressed as (Van Bavel 1976, Saito 2006):

$$R_n - H - \lambda E - G = 0$$ Eqn. 16

Where R_n is net radiation (incoming-outgoing SWR and LWR)(W·m^{-2}), G is heat flux into the ground (W·m^{-2}), H is sensible heat flux outwards (W·m^{-2}), and λE is latent heat flux outward via evaporation (W·m^{-2}). This method may be suitable over long time scales, or when considering a single moment, but assuming no advection or storage of energy is problematic. One potential solution is to use software such as Hydrus 1D to balance these static variables for each time step with a time-variable boundary condition.

Hydrus 1D partitions net radiation based on the following formula (Šimůnek 2005):

$$R_n = R_{ns} + R_{nl} = (1 - \alpha)R_s + \{[(1 - 0.84c) \cdot \varepsilon_a + 0.84c]\sigma T_a^4 - \varepsilon_s \sigma T_s^4\}$$

Eqn. 17

Where R_{ns} is net shortwave radiation (W·m^{-2}), R_{nl} is net longwave radiation (W·m^{-2}), α is surface albedo [1], R_s is incoming solar radiation (W·m^{-2}), ε_a is the atmospheric emissivity

of clear sky [1], ε_s is soil emissivity [1], c is cloud cover fraction [1], σ is the Stephan-Boltzmann constant, T_a is air temperature (K), and T_s is soil surface temperature (K).

Latent heat flux is calculated as the product of evaporation rate with the latent heat of vaporization. Hydrus defines evaporation according to Camillo and Gurney's (1986) model:

$$E = \frac{\rho_s - \rho_a}{r_a + r_s} \qquad \text{Eqn. 18}$$

Where ρ_s is vapor density at the soil surface (kg·m^{-3}), ρ_a is atmospheric vapor density (kg·m^{-3}), and r_a and r_s are aerodynamic resistance and soil surface resistance to vapor flow, respectively (s·m^{-1}).

Hydrus calculates sensible heat flux as defined by Van Bavel (1976):

$$H = C_a \frac{T_s - T_a}{r_h} \qquad \text{Eqn. 19}$$

Where C_a is the volumetric heat capacity of air (J·m^{-3}·K^{-1}), T_s is surface temperature (K), T_a is air temperature (K), and r_h is the aerodynamic resistance to heat transfer (s·m^{-1}). r_h is assumed to equal r_a.

Other than these equations for estimating the surface energy balance and potential evaporation, Hydrus 1D functions essentially the same way as Hydrus 2D. More information on the Hydrus software can be found in the published user manuals, the internal help files, and from the online Hydrus forums.

<u>Previous Work</u>

In any natural setting, the rising and setting of the sun plus variable cloud cover creates a periodic fluctuation in incoming SWR at the ground surface. Subsequently, the ground surface warms and cools in a similar pattern, dependent on the thermal properties

of the soil and ground cover. The cyclical nature of this effect poses a problem for the efficient use of thermal sensing and for effectively capturing temperature variations in a shallow subsurface model (Šimůnek et al. 2001). Since some landmines store and release heat at different rates than soil, landmines are often warmer than the surrounding soil at night and cooler during the day (Bruschini 1997). This transition between warming and cooling periods means that under dry conditions there are two periods each day of maximum thermal contrast between landmines and soil, and two periods where that contrast is negligible (Bruschini 1997, Šimůnek et al. 2001). Accurate thermal detection may then require at least 12-24 hours of monitoring to account for diurnal temperature cycles (van Dam 2005, Šimůnek 2001). This timing constraint on thermal sensing is motivation to examine whether the presence of water above a landmine can extend the time frame of possible thermal detection.

Wet soils have higher density, specific heat, thermal conductivity, and thermal diffusivity than dry soils. This means that wet soil can store more heat, but also that it can transmit heat more effectively. This also means dry soils will experience larger variation in surface temperature compared to wet soil, since wet soil is slower to respond to diurnal radiation variations (Dzerko 2012). In general, soil thermal signal is damped in wet and humid climates (van Dam 2003).

Though wet soil temperature may not vary as much as for dry soil, thermal contrast between the soil above a buried object and the surrounding soil is crucial to consider, not just the magnitude of temperature fluctuations. A wet soil is more able to retain heat, so the surface of a wet soil maintains higher temperature at night. Water content controls the timing of peak surface thermal signature (van Dam 2003). Water perched above and around

a buried object may then expand the timeframe of surface thermal contrast compared to dry surroundings. Das et al. (2001) suggests modeling as a good approach to determine optimal timing of thermal mine detection. Thermal diffusivity is also central to the timing of surface thermal contrast between buried objects and surrounding soil. As indicated by the results of Smits et al. (2013), objects with high κ may equilibrate thermally with soil too quickly to be detected under dry or wet conditions.

Landmine depth is another factor tied to the problem of diurnal temperature signals. Stallman (1965) shows that, as a temperature signal propagates into the ground, the amplitude is damped and the signal is phase shifted. The degree of thermal wave attenuation at depth depends on thermal conductivity, specific heat, and density, all of which are represented by thermal diffusivity (Stallman 1965). When fluid is the advective conduit of heat into the soil, infiltration rate and the fluid thermal properties also affect the wave attenuation. By altering the hydraulic response of a soil, mine depth and resultant changes in water retention may also influence the timing of maximum thermal contrast (van Dam 2003). Anti-personnel mines are typically buried flush with the ground surface or up to 10 cm depth, while anti-tank mines are usually buried up to 20 cm depth (Donskoy 2002). Though exact estimates vary, some authors suggest that diurnal temperature signatures only penetrate the upper 15 cm, in the vicinity of typical mine burial (Smits 2013, Garcia-Padron 2002, Šimůnek 2001). While natural temperature amplitude is smaller for wet soils, the minimum signature depth can be increased by higher VWC (van Dam 2005).

The obstruction of fluid flow by a buried object causes differences in water content around the object relative to its surroundings (Bouwer and Rice 1984). I demonstrated this

effect previously using Hydrus 2D for coursework at the University of Nevada Reno. An example of the results is shown in Figure 3, which depicts a body of sand initially at 20% VWC allowed to drain freely. The image is a snapshot 3 hours into the simulation, showing a zone of increased soil moisture ponded over an impermeable buried object at 10 cm depth and a zone of reduced soil moisture below the object. Das et al. (2001) observed similar distributions surrounding landmines during wet conditions. For dry conditions, Das at al. (2001) also report the reverse soil moisture distribution, with wetter soil below the mine and drier soil above the mine, compared to adjacent soil.

In general, Das et al. (2001) found greater variation in soil water content surrounding landmines than away from them. Smits et al. (2013) note that moisture and temperature variations around buried objects change depending on mine depth. During dry conditions, increased soil moisture ponded above an object may provide more potential for evaporation, and thus greater thermal exchange by latent heat flux. This latent heat flux may in turn increase the relative surface temperature signal with respect to the surrounding surface, however increased water content will also dampen the amplitude of temperature fluctuations relative to dry soil. The magnitude of water content contrast above and adjacent to a mine will also depend on the magnitude and timing of precipitation events (Das 2001).
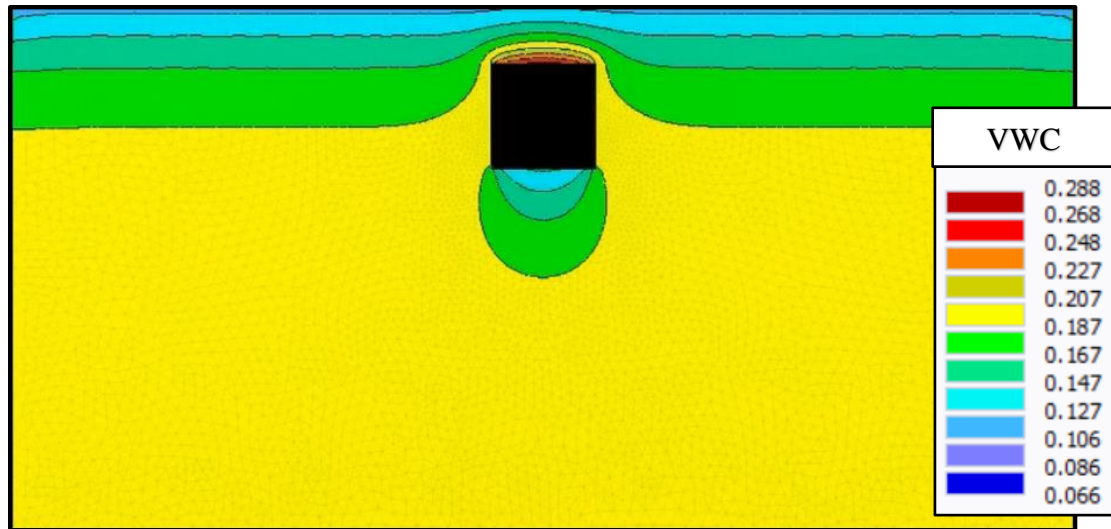
Figure 3: Hydrus 2D simulation of a 1m deep, 2m wide sand that started 20% volumetric content and could drain freely. This snapshot is 3 hours into the simulation, showing ponding of soil moisture above a square object defined by no-flow boundaries. There is also a zone of diminished water content below the modeled object. Each color change represents an approximate 2% change in water content, with dark red representing 28.8% water content.

Several authors have suggested soil watering to boost thermal sensor performance (Das et al. 2001, Šimůnek 2001, Hong 2001). Smits et al. (2013) report that elevated soil moisture usually increases the maximum thermal signature above a target, but found this was not true for simulated aluminum and lead mine compositions. These two cases showed a diminished thermal signature due to high thermal diffusivity of the targets, allowing rapid thermal equilibrium with the surrounding soil. Accurate representation of landmine thermal properties is therefore necessary since higher thermal conductivity of a target may diminish surface thermal signature (Smits 2013, van Dam 2005).

Soil is disturbed during landmine burial, which may have an effect on physical properties of a soil. Research on the effects of soil disturbance on the thermal and hydraulic properties of soil is limited. Soil disturbance disrupts natural soil horizons formed during pedogenesis, disorients clay particles, decreases bulk density, and increases porosity (Caldwell 2012, Das 2001). McDonald et al. (2015) found that thermal diffusivity of undisturbed soils in a U.S. Army testing facility was consistently around 10-15% lower than for disturbed samples. They also note that these differences may be conservative since soils tested were weakly developed, and the "undisturbed" surfaces are regularly raked in between testing operations. We would expect that a weakly developed soil or one with low cohesion (such as a loose sand) would maintain similar physical properties following disturbance, with the difference being driven largely by the repacking of the soil following disturbance. Bruschini (1997) suggests that surface effects from soil disturbance may be detectable for weeks, though there is little more mention of the timing of soil disturbance in the literature.

In the context of landmine detection, there have been many studies focused on sensor response, though few that consider the effects of soil moisture and heat dynamics in soil (Smits 2013). Research that compares modeled, field, and laboratory studies are also rare. Das et al. (2001) and Šimůnek et al. (2001) both used Hydrus models to compare surface temperature records from Bosnia and Kuwait for various conditions to study water distributions and temperature distributions, respectively. The research of Das et al. (2001) was limited to only medium-textured soil types (no sands or impermeable clays). Šimůnek et al (2001) focused on heat transport surrounding landmines, but considered water content to be a static variable. Smits et al. (2013) present physical experiments of water and heat

flow in a quasi-two-dimensional laboratory model, which was then fed into a COMSOL finite element digital model to compare variations in target thermal properties. Despite the rigorous treatment of this experiment, its application is limited since only one type of sand and one type of target were examined. Here I examine digital models of laboratory experiments, focusing on the dynamics of heat and water flow in variably-saturated sand under a range of controlled and natural environmental conditions.

Hypotheses

1. HYDRUS 2D can be used to generate to simulate surface temperature associated with the flow of water and heat around a buried, impermeable object.

2. If not, HYDRUS 1D modeling can supplement the 2D model to account for the surface energy budget, including latent and radiant heat terms.

These hypotheses are meant to be interpreted in context of the research questions described in the introduction of this paper. Specifically:

1. What role do transient soil water flows play in controlling surface temperatures above shallowly buried objects?

2. Do the thermal properties of a buried object influence the surface thermal signature?

Methods

The approach of this study is to use controlled experiments and to generate data-validated Hydrus models capable of running simulations of varied soil and environmental conditions. This section begins with description of the experimental setup created in an indoor controlled environment at the Desert Research Institute (DRI) in Reno, Nevada.

This is followed by description of field experiments conducted in a similar fashion to those in the lab, but in a natural environment at the Yuma Proving Grounds in Yuma, AZ (MERS South). Both experiments were designed and constructed to examine the interactions between water and heat flow around buried landmines and mine-like objects.

<div align="center">EcoCELL Test Development</div>

Physical experiments were constructed at the DRI Frits Went Laboratory glasshouse, a large, windowed, south-facing greenhouse facility. Within the laboratory, there are several smaller windowed units called EcoCELLs (Ecologically Controlled Enclosed Lysimeter Laboratories). For this study and related research, one EcoCELL containing two soil plots was dedicated to our experiments. Each soil plot is encased in reinforced concrete, measuring 1.22 m wide, 2.44 m long, and 1.74 m deep on the interior. The soil surface is 9-10 cm from the top of the concrete box, so soil depth is approximately 1.65 m. Initially, each plot initially contained an intact core of a native soil from Oklahoma (OK) that has a clay-loam texture.

Two target types were fabricated for these experiments, with duplicates made for each soil type. The first (Target A) is a red 2 ½ gallon plastic gas can filled with granular ammonium nitrate fertilizer, a common component of improvised explosives. The dimensions of the can are 30.5 cm deep, 30.5 cm long, and 21 cm wide, ignoring the handle. The second target (Target B) is a 30.5 cm long, 16.5 cm diameter steel cylinder, filled with dry sand, and capped by two flat disks welded on at each end. Sand was selected for its similar thermal properties and density to high explosive (Baytos 1979). Šimůnek et al (2001) point out that TNT has a thermal conductivity close to oven-dry sand, but volumetric heat capacity closer to wet soil.

We used ECH20 5TE (Meter Group, Pullman, Washington) probes for these experiments to measure temperature, electrical conductivity, and apparent dielectric permittivity. Dielectric permittivity is converted to volumetric water content by applying the Topp equation (Topp et al. 1980):

$$\theta \left(\frac{m^3}{m^3}\right) = 4.3 \times 10^{-6} \varepsilon_a^3 - 5.5 \times 10^{-4} \varepsilon_a^2 + 2.92 \times 10^{-2} \varepsilon_a^{-5.3 \times 10^{-2}} \quad \text{Eqn. 20}$$

Where ε_a is apparent dielectric permittivity [1], a unitless value representing the ratio of conductive properties of a material to that of a vacuum. Dielectric permittivity, the ratio of conductive properties of a material to that of a vacuum, equals 1 for air and 80 for water (Radcliffe & Šimůnek 2010). Relative permittivity of dry soils is generally low (around 4 for sandy soil, Robinson et al. 1999), so ε_a can often be used to infer soil water content. Volumetric water content measurement resolution of the 5TE probes is 0.1% from 1-20 percent VWC, and <0.75% from 20-80 percent VWC (Decagon Devices 2010). When using the Topp equation to calculate VWC from apparent dielectric permittivity, the accuracy of the 5TE probes is ±1 to 2% VWC (Decagon Devices 2010). Bulk electrical conductivity measurements range from 0-23 dS/m, with 0.01-0.05 dS/m resolution and ±10% accuracy. Temperature can be measured from -40°C to 60°C, with 0.1°C resolution and ±1°C accuracy (Decagon Devices 2010). The 5TE sensors are 10 cm long, 3.2 cm wide, and 0.7 cm thick, with three 5.2 cm prongs. Measurement output is configured to SDI-12 and recorded using a CR3000 datalogger (Campbell Scientific, Logan, Utah).

Half (vertically) of each plot was excavated using hand tools and a hammer-drill with a spade bit (Figure 4A). The excavated side of each plot was filled with Quikrete Medium Sand, a commercially available, uniform, medium, dry sand selected for

uniformity and bulk cost (Figure 4B). The predominant grain size range reported for Quikrete Medium Sand is 0.3-0.8 mm (Quikrete Companies LLC, 2018). A small square tile was placed over the drain that underlies the sand columns, to allow only water to drain without sand loss (Figure 4A). The sand was periodically leveled and compacted while filling the plots to maintain uniform density. An EGauge Model 4590 soil density gauge was used at the surface of the sand plots to measure density and water content once targets and sensors were placed (Troxler, Research Triangle Park, NC). Density was measured to be about 1.6 kg/m^3 (Table 1). Table 1 also includes density measurements for the MERS sites described in the following section. Approximately 4000 kg of sand was used to fill the two plots.

Figure 4: Panel A shows the EcoCELL plot with half of the OK soil excavated. Note the small tile placed over the drain to prevent loss of sand. Panel B shows placement of Target A and three sensors during the filling process. Panel C shows the completed experimental setup, with sensor cables routed through PVC piping to a data logger. Note the insulating foam which surrounds the soil plots.

Soil Plot	Moisture (%)	Average Wet Density (kg/m^3)	Average Dry Density (kg/m^3)
North EcoCELL Sand (100mm)	1.2-1.5	1.61	1.59
North EcoCELL Sand (200mm)	1.2-1.5	1.63	1.60
South EcoCELL Sand (100mm)	1.3 - 1.6	1.63	1.61
South EcoCELL Sand (200mm)	1.3 - 1.6	1.64	1.62
MERS South Native (1/4) (100mm)	4.2-4.8	1.79	1.71
MERS South Native (1/4) (200mm)	4.0-4.8	1.82	1.72
MERS South Sand (2/4) (100mm)	2.0-2.3	1.49	1.46
MERS South Sand (2/4) (200mm)	2.0-2.2	1.5	1.47

Table 1: Troxler moisture and density measurements for EcoCELL sand plots and for two of four MERS site plots. All values collected immediately following construction.

Targets and sensors were placed in the sand as each plot was filled. Sensors were oriented in a N-S plane around each target at varied distances to capture the greatest range of distances horizontally and vertically. All sensors were placed horizontally to minimize the formation of preferential hydraulic flow paths. Three sensors were placed below each target at 139.7 cm, 73.7cm, and 48.3 cm depth (sensors G, F, and E, respectively). Sensor E lies 2.5 cm below Target A. Target A was placed next, with three more sensors placed at half the height of the target. Sensors C, D, and B were spaced 17.8 cm, 33.0 cm, and 43.2 cm to the side of Target A, respectively, with Sensor B alone to the north. The last sensor, Sensor A, was placed halfway between the top of Target A and the soil surface at 7.6 cm depth (Figure 5). Sensor cables were routed to the corner of each plot and through PVC piping to the surface.
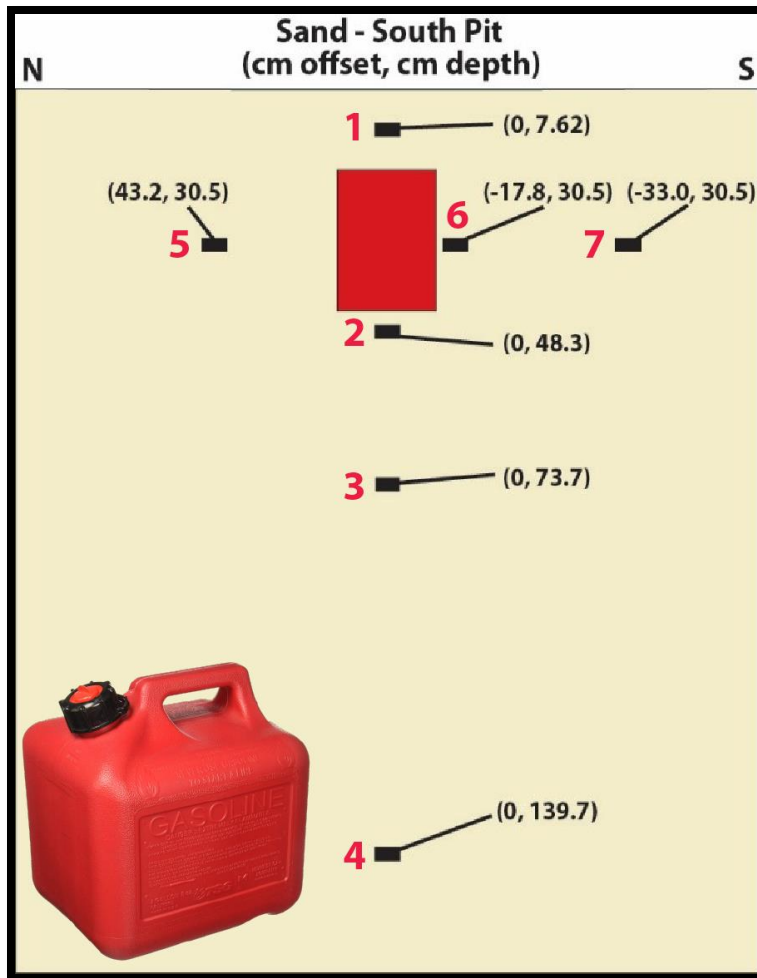
Figure 5: Sensor layouts for the South Sand EcoCELL experiment. Sensor positions are listed with N-S offset from center, and depth (cm). Sensor IDs are shown in red. The red rectangle represents Target A, pictured in the corner.

Measurements for all 5TE sensors were every hour from 5/19/18 to present. Air temperature and relative humidity are recorded hourly. Since testing began, the EcoCELL climate has been controlled to simulate four long-term environmental treatments. From 5/19/18 to 8/27/19 the experiments were run in a "desert" climate (Hot/Dry), with dry soil, repeating high daily temperature fluctuations, and humidity as low as possible. On 8/27/18 saturating the soil began, marking the beginning of the "warm temperate" phase (Hot/Wet),

with the same high air temperature, wet soil, and higher humidity. Water was added to the sand for 30 minutes, twice a day. By 12/4/18 a total of 2,221 gallons through the sand. On 12/4/18 the system was cooled and the "cold temperate" phase began (Cold/Wet). For this scenario, the cells were cooled to ambient temperatures. On 4/22/19 the water was turned off, allowing the system to dry out and beginning the final "warm dry" phase. For this study, data from the first three scenarios are used.

YPG Master Environmental Reference Site Field Experiments

In November 2018, field experiments were constructed at the countermine facility of the U.S. Army Yuma Proving Ground (YPG), a military testing facility 30 miles northeast of Yuma, Arizona. The site was selected to utilize a Master Environmental Reference Site (MERS) already in place. The MERS stations are a network of fully instrumented meteorological stations set up by DRI researchers, capable of measuring precipitation, wind speed, incoming and outgoing longwave and shortwave radiation, relative humidity, barometric pressure, and air temperature - all the variables necessary to accurately calculate potential evaporation (McDonald 2013).

For this study, soil data from the YPG site is not analyzed, but the meteorological data collected from the MERS station is used. This is explained in the section on Hydrus 1D modeling.

The YPG MERS station measures incoming and outgoing, shortwave and longwave radiation using a CNR1 net radiometer (Campbell Scientific, Logan, Utah). Ground surface temperature is measured using an SI-111 infrared radiometer (Campbell Scientific, Logan, Utah). Air temperature and relative humidity are measured using a HMP45C temperature and relative humidity probe (Campbell Scientific, Logan, Utah).

Wind speed and direction is measured by a 034B wind sensor (Met One, Grants Pass, OR).

Sensor range and accuracy is presented in Table 2. Sensor data is logged on a CR3000

datalogger (Campbell Scientific, Logan, Utah).

Sensor Description	Model	Units	Range	Accuracy
Air Temperature	HMP45C	°C	-40 to 60	± 0.5°C
Relative Humidity	HMP45C	%	0 to 100	± 2% (0-90%) ± 3% (90-100%)
Wind Speed	034B	m/s	0 to 75	0.1 m/s (<10.14 m/s) ± 1.1 m/s (>10.14 m/s)
Soil Surface Temperature	SI-111	°C	-55 to 80	± 0.2°C (-10 to 65°C)
Incoming SWR	CNR1	W^1m^{-2}	305 to 2800 nm	± 10% of daily sums
Outgoing SWR	CNR1	W^1m^{-2}	305 to 2800 nm	± 10% of daily sums
Incoming LWR	CNR1	W^1m^{-2}	5 to 50 nm	± 10% of daily sums
Outgoing LWR	CNR1	W^1m^{-2}	5 to 50 nm	± 10% of daily sums

Table 2: Range and accuracy specifications for the meteorological sensors deployed at the YPG MERS location.

Hydrus 2D Model Domain Properties and Initial Construction

This section details the modeling process using Hydrus, software developed at UC

Riverside for simulating water, heat, and solute transport in the vadose zone. The southern

sand (SS) EcoCELL plot containing the gas can of ammonium nitrate (Target A) was the

only soil unit selected for modeling for three reasons. First, the sand is less complicated

than the OK soil, given that the OK soil was disturbed during target and sensor placement.

Given the uniformity of the sand, thermal and hydrologic effects of organic material were

omitted from modeling, and effects of soil heterogeneity are assumed to be averaged over

the experimental domain so that the soil could be represented as a single homogeneous

unit. Second, Target A was assumed to have improved water retention relative to Target B,

owing to its flat top. Third, the 140 cm depth sensors in both sand plots returned unreliable

data for most of the duration of the experiments, but the Target A sand plot was selected

since it provided a wider spatial distribution of data compared to the Target B sand plot. The focus of these experiments is on the heat and water flow at the soil surface and around the targets, so the loss of the deepest sensor is not critical.

The Hydrus model domain was scaled to the nearest 1 cm match to the dimensions of the EcoCELL plots, with a width of 122 cm and soil depth of 165 cm. Target A has a width of 21 cm, a height of 32 cm, and a burial depth of 15 cm. Sensors were modeled as observation points at the center of each sensor position, with the assumption that the sensors themselves do not disrupt water and heat flow.

To allow for heat transport, but not water flow, an area with the dimensions of Target A was cut from the model domain and filled with a second surface assigned to material 2, ammonium nitrate. Since the ammonium nitrate remains dry, its hydraulic conductivity was set to 1×10^{-15} cm/hr to effectively eliminate water flow between the sand and the ammonium nitrate, while allowing for conductive heat exchange and heat storage. No water flow between the sand and ammonium nitrate was observed, and Target A maintained a thermal connection to its surroundings.

The base of the SS EcoCELL plot is uninsulated metal, with a small drain covered by a raised tile to prevent clogging and soil loss. The bottom boundary was modeled as a no-flow boundary with a 10 cm wide opening representing the restricted water flow. Here, the lower boundary condition (LBC) was set to a variable flux boundary corresponding to the drainage output when run as a seepage face boundary (drains when saturated). The side of the model domain were set to no-flow boundary conditions for water and heat.

The sizing of the finite element mesh was refined to 1 cm spacing along the soil surface, with the target surface refined to 2 cm. Sensors were represented as observation

points at the center of each 5TE placement, and have a 2 cm grid refinement. Otherwise, global grid refinement was set to the default of 5.1 cm, resulting in a total of almost 6,000 nodes - a comparable grid density to the models of Šimůnek et al. (2001) and Das et al. (2001).

The sand model was initially run without heat, and was run in a steady-state mode to test the functionality of boundary conditions without inverse optimization of parameters. A purely water flow model was used to constrain the hydraulic parameters. Hydraulic parameters were estimated before heat parameters to simplify the water models. Default water content tolerances were used, with a minimum timestep set to 1 second. A persistent problem with the forward modeling was handling the transition from completely dry soil to suddenly saturated soil, once watering began on 8/28/18. To help smooth transitions in water content, the option to interpolate time variable boundary conditions in time was selected, but was eventually removed. This choice had minimal effect on the total water budget since variable flux data was input at 5-minute intervals.

The 5TE sensor data was cleaned of all unreliable data. If only one sensor behaved erroneously, it was assumed this did not influence the other sensors, and the other data was preserved. For each sensor, water content data was considered unreliable if the corresponding temperature data was bad, and vice versa. If reported water content exceeded saturated water content, then that data was omitted. The Sensor G (139.7 cm depth) record was omitted from all calibration and validation data sets for lack of available, trustworthy data. Sensor C (17.8 cm offset, 30.5 cm depth) was omitted from water flow calibration for lack of data.

Several sections of the data were omitted from calibration and validation datasets, though watering schedule (variable flux boundary) and the upper time-variable heat boundary condition did use data from these periods to maintain energy and mass balance. Though air temperature in the EcoCELLs is controlled, soil temperature took time to equilibrate. For the water flow parameterization, the front end of the sensor record (5/20/18 – 6/25/18) was omitted from calibration and validation to avoid the extra complexity of a warming system. The period after irrigation began (8/28/18 – 10/15/18) was particularly rife with spotty data and overestimation of water content, so it was not used. The transition from hot conditions to cold conditions (12/5/18 – 12/15/18) was also skipped. The cleaned data for the south sand EcoCELL plot and calibration and validation periods for the water flow modeling are shown in Figure 6.

The UBC for water flow was set as a variable flux condition. After two weeks of increased watering to saturate the soil columns, soil watering followed a regular schedule beginning on 8/27/18 and ending on 4/22/19. Each plot was watered for 30 minutes every day at 7 AM, and on 11/8/18, the sand plots began receiving an additional 30 minutes of watering at 2 PM. Water was delivered at 2 liters per minute for each plot, which equates to 8 cm/hr into the soil. Initial conditions of sand water content were taken directly from the data, and closely matched a linear distribution between specified top and bottom values.

Van Genuchten hydraulic flow parameters were determined through lab measurement, inverse modeling, direct observation, and literature values. Parameters were first tested using a HYPROP (Meter Group, Pullman, Washington) that measures changes in water potential with changes in water content to create a soil water retention curve (UMS

2015). Model parameters not sufficiently constrained experimentally were determined using inverse modeling.

The hydraulic parameters of the ammonium nitrate were set to that of the Hydrus catalog sand, except residual water content was set to 1%. Initial water content in the ammonium nitrate was fixed at 3% for all models. Hydraulic conductivity of the ammonium nitrate was set to 10^{-15} cm/hr.

Total porosity of soil and ammonium-nitrate were measured in the DRI soils lab using a graduated cylinder and scale. 300mL of oven dried material was saturated with water, the initial weight subtracted from the final weight to get the weight of water added and thus the volume of water added. This pore volume divided by the total volume gives approximate porosity, which is the compliment of solid fraction. The solid fraction for sand is 0.622 and for ammonium nitrate is 0.644. The ammonium nitrate pellets did not dissolve during this quick procedure.

Water content distributions were modeled for the EcoCELL South Sand for three of the four controlled climate tests, from 6/25/18 to 4/13/2019. Model iteration criteria, finite element mesh refinement, and domain boundary conditions were represented by the model, but not evaporation. Both directly measured flow parameters and Hydrus catalog sand parameters were used as initial values, which were then optimized using inverse modeling. The objective function used by Hydrus for inverse modeling is meant to minimize discrepancy between observed data and modeled values by adjusting specified parameters within specified bounds (Šimůnek 2005, page 129). The initial conditions and objective function bounds used for Van Genuchten flow parameters are presented in Table 3. Only K_S was given an objective function upper bound.
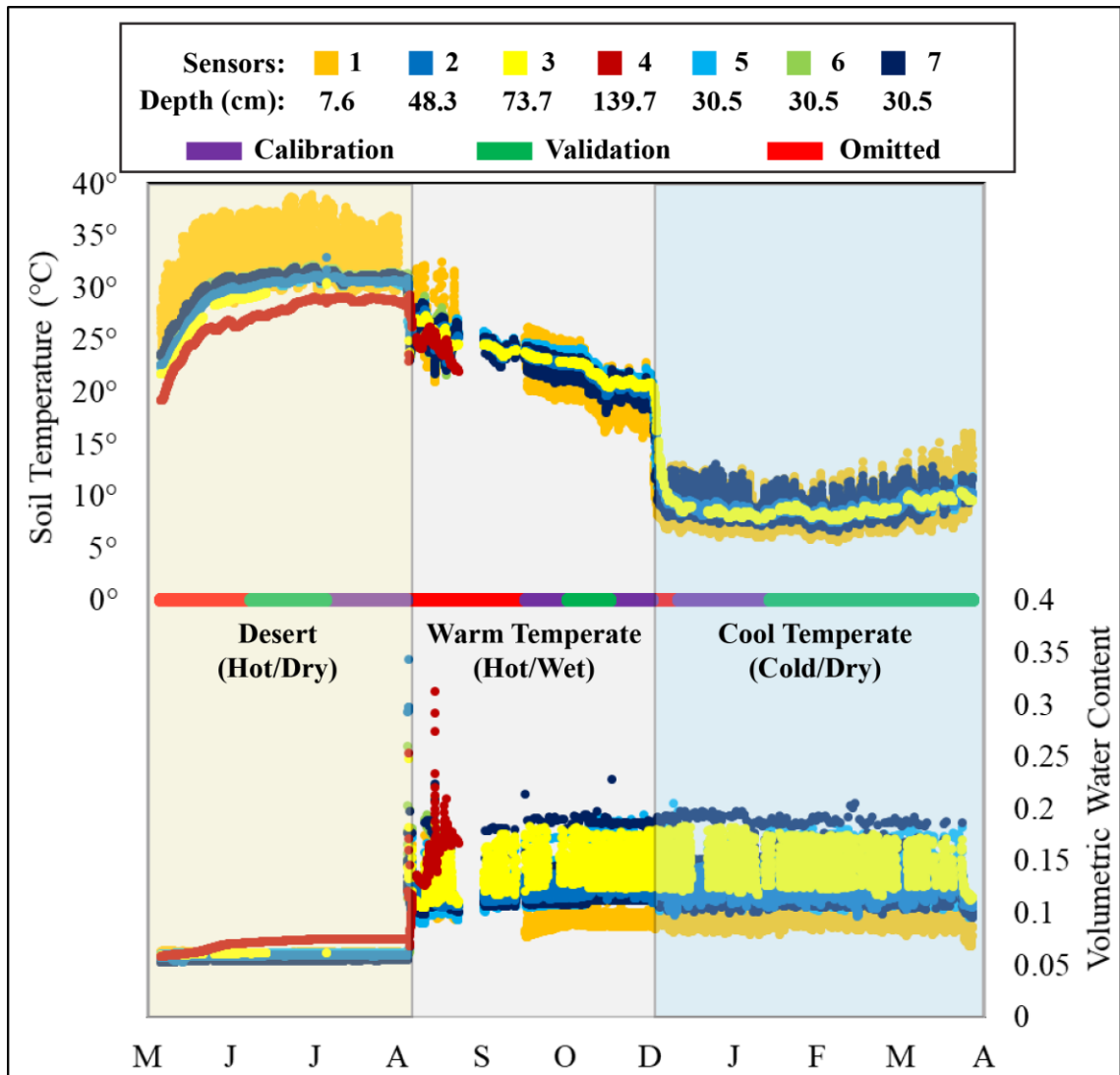
Figure 6: Time series of cleaned soil temperature and water content data for the south sand EcoCELL plot for the Desert, Warm Temperate, and Cold Temperate experiments. Sensor IDs and positions are shown in Figure 5. In the top plot, note the increased diurnal temperature signal in the Sensor 1 record (orange), and the truncated record of Sensor 4 (dark red). For the bottom plot, water contents above 40% are considered outliers and have been removed. The center line dividing the two plots is colored based on which portions for used for calibration, for validation, or omitted. The initial spin-up time of the experiment is omitted, as well as both transition periods.

Flow Parameter	Units	Initial Condition	Lower Bound	Upper Bound
Residual Water Content	(m³m⁻³)	0.045	-	-
Saturated Water Content	(m³m⁻³)	0.365	-	-
alpha	[1]	0.0427	-	-
n	cm⁻¹	3	-	-
Sat. Hydraulic Conductivity	cm/day	29.7	0	1000

Table 3: Initial conditions and bounds used to constrain optimization of the Van Genuchten water flow parameters in Hydrus 2D water flow model. Dashes represent unconstrained bounds for the Hydrus objective function.

For each sensor, the statistical metrics used to quantify fit are mean error (ME), mean absolute error (MAE), root mean squared error (RMSE), R-squared, and the RMSE minus the absolute value of mean error. $RMSE - |ME|$ can be considered a measure of model precision. Hydrus outputs residuals (observed value minus predicted value) for each observed data point that is fed into an inverse model. With these residuals, the statistical metrics are calculated as follows:

$$Mean\ Error\ (ME) = \frac{1}{n}\sum_{i=1}^{n} Observed - Predicted \qquad \text{Eqn. 21}$$

$$Mean\ Absolute\ Error\ (MAE) = \frac{1}{n}\sum_{i=1}^{n}|Observed - Predicted| \quad \text{Eqn. 22}$$

$$RMSE = \sqrt{\frac{\sum_{i=1}^{n}(Observed - Predicted)^2}{n}} \qquad \text{Eqn. 23}$$

Hydrus 2D Heat Modeling

Heat flow for the EcoCELL sand plot was modeled using the same domain geometry as the water flow models, and with the calibrated hydraulic parameters fixed. As with the water flow model, the effects of organic material on heat flow were assumed to be negligible. Unlike the water flow model, only the desert (Hot/Dry) controlled climate

period was used to constrain heat transport parameters. The absence of water flow meant the conductive parameters were isolated, with minimal advective heat transport. Portions of the hot/dry period (5/20/18 – 8/28/18) were selected for calibration and validation such that over one third of the dataset was reserved for validation, as with the water flow model. Two sections of data used for validation bookend the calibration data (Figure 7).
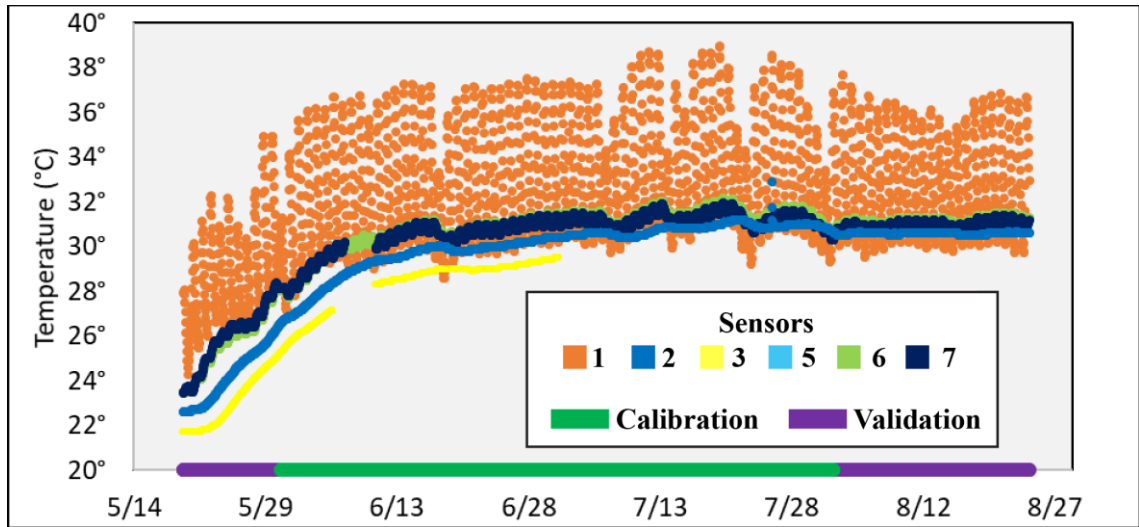
Figure 7: Temperature record used for constraining heat transport parameters in Hydrus 2D model. Calibration data is underlined in purple. Validation data is underlined in green. Sensor 1 data was modified for use as an upper boundary condition, and not used for calibration or validation.

Without the ability to model surface energy balance using Hydrus 2D, or to estimate potential evaporation, the 2D heat modeling was focused solely on heat conducted between water, sand, and the target. For determining thermal conductivity, $\lambda(\theta)$, the Chung and Horton (1987) model is used:

$$\lambda_0(\theta) = b_1 + b_2\theta + b_3\theta^{0.5} \qquad \text{Eqn. 24}$$

Where b_1, b_2, and b_3 are empirical parameters (Šimůnek et al. 2006). Table 4 contains b-parameters for estimating apparent thermal conductivity specified by Chung and Horton, and Figure 8 shows those parameters plotted over the full range of volumetric water content.

Soil Type	b1	b2	b3
Sand	0.228	-2.406	4.909
Loam	0.243	0.393	1.534
Clay	-0.197	-0.962	2.521

Table 4: Typical values of Chung and Horton b-parameters for different soil types
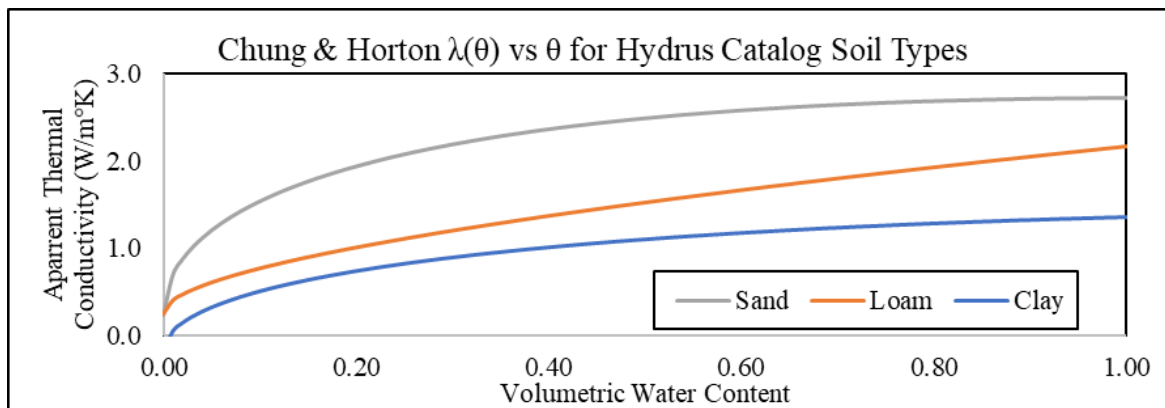
Figure 8: Thermal conductivity curves from the Chung and Horton (1985) model for sand, loam, and clay. Fitting parameters used are the default Hydrus for the three soil types.

The Hydrus heat parameters are the Chung and Horton b-parameters (Eqn. 21), volumetric heat capacity of soil, volumetric heat capacity of water, and volumetric heat capacity of organic material. Organic solid fraction was set to zero, and the volumetric heat capacities of water and silica sand were fixed for these experiments; bulk volumetric heat capacity is determined as a linear combination of the solid and water fractions (neglecting the heat capacity of air). It is assumed that temperature dependence of water flow is negligible over the range of modeled temperatures, so this scaling was omitted from the modeling.

Thermal conductivity and volumetric heat capacity was measured using a KD2-Pro Thermal Properties Analyzer (Meter Group, Pullman, Washington). A known volume of sand was baked at 105°C for 24 hours, then water was added in increments of 3% volumetric water content from 0 to 39%. At 39% water content, the sand was oversaturated and exactly 2.5% volumetric water content decanted, leaving 36.5% saturated water content, and confirming the HYPROP estimate. Thermal conductivity was measured four to eight times at each step. Average values for each step were then plotted, and far closer estimates for b2 and b3 parameters found by solving Equation 24 and manually tuning the b-parameters. Fitted b-parameters are shown in Figure 9, including the curve from previous initial conditions tested using the Chung and Horton estimates for sand.
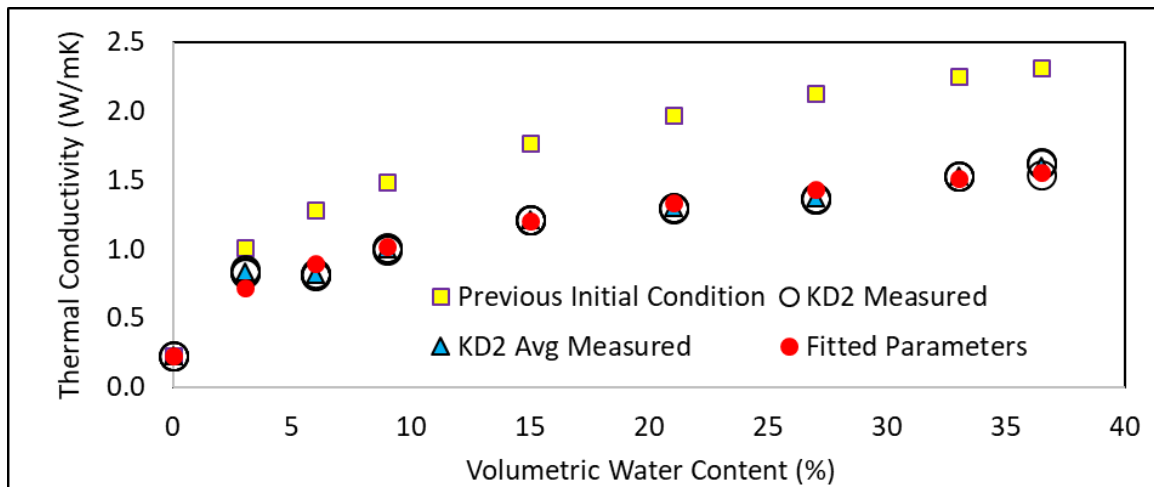
Figure 9: Lab tested thermal conductivity values for EcoCELL sand for every 3% volumetric water content. Results were used to manually fit the Chung and Horton b2 and b3 parameters.

The next modeling step was to adjust the boundary conditions to optimize the model fit. Since surface temperature was not directly measured and Hydrus 2D does not allow for

an energy balance UBC, surface temperature was extrapolated from the Sensor 1 (8 cm depth) temperature record based on exponential attenuation of the periodic diurnal temperature signals across all sensors. To match the hourly timestep of the soil temperature record to that of the 5 minute watering record, each temperature datum was repeated 12 times. Sensor 1 data gaps were filled linearly (where gaps had a short duration), or filled by matching a sinusoid of equivalent amplitude to the record before and after the gap (Figures 10 & 11).

Diurnal temperature fluctuations at the surface become increasingly lagged and damped with depth in soils (Stallman 1965). Temperature amplitude decreases exponentially with depth, so by assuming minimal phase shift of peak temperatures, surface temperature amplitude was extrapolated from the change in amplitudes across the range of sensors (Figure 12). A scaling multiplier of 1.7 was applied to the Sensor 1 record, which was then used as a specified time-variable UBC for heat. The LBC was a fixed temperature of 21 °C for the hot treatments and 5 °C for the cold treatments.
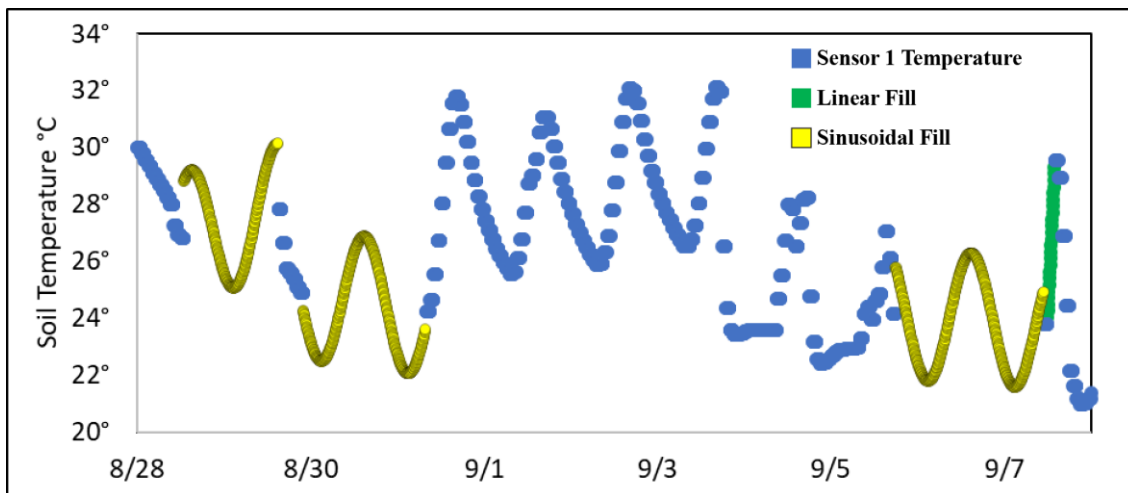
Figure 10: Sample section of artificial fill to represent diurnal temperature signal for Sensor 1 (the shallowest sensor). Hourly data repeated to approximate 5-minute data is blue, linearly filled data is green, and sinusoidally filled data is yellow.
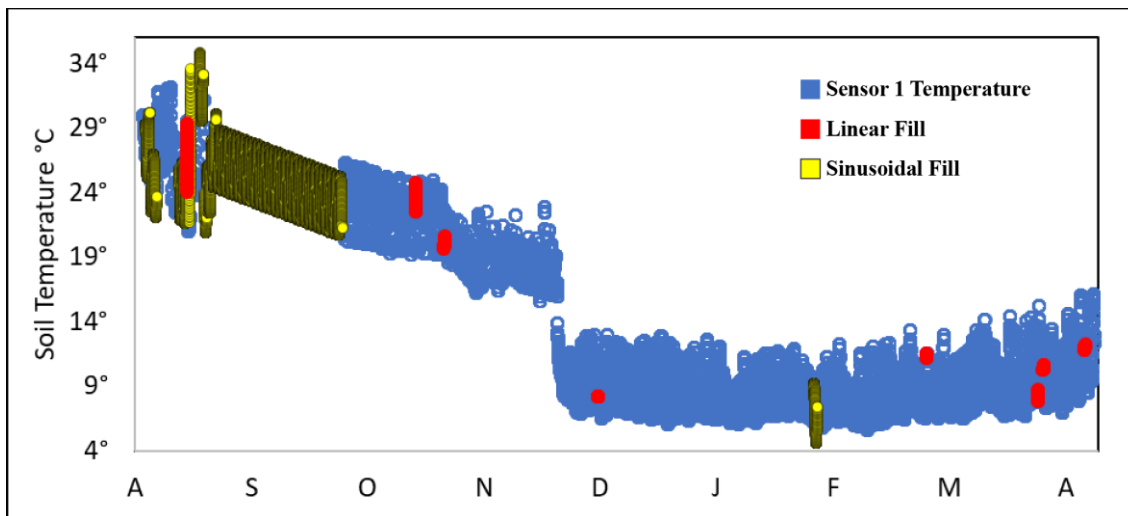
Figure 11: Filled temperature record for the 3-in depth south sand sensor during the wet stages of the EcoCELL experiments. Observed data are blue, sinusoidally filled data are yellow, and linearly filled data are red.
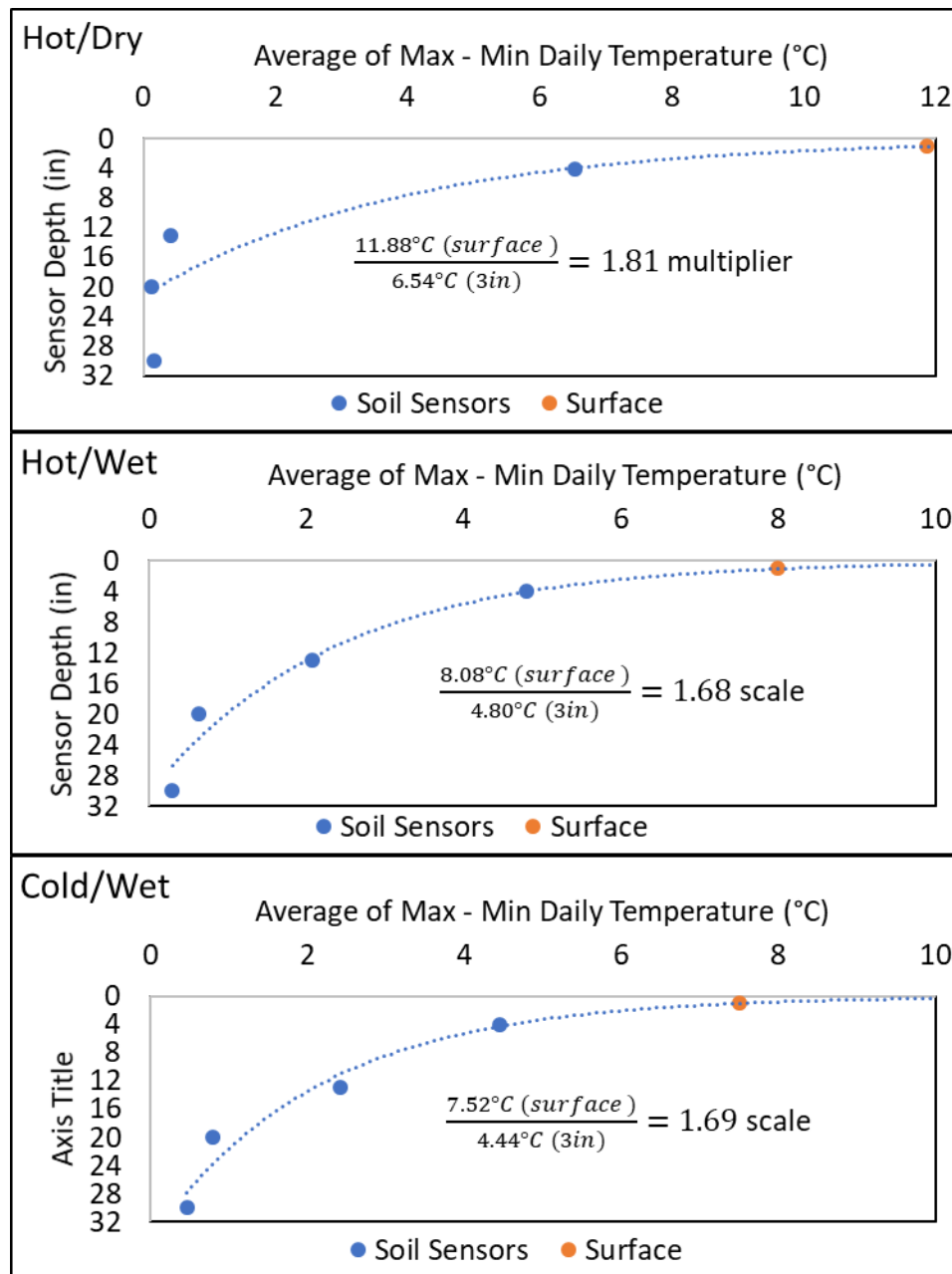
Figure 12: Average daily temperature variations (Max-Min) for each sensor depth, compared between controlled climate experiments. An exponential trendline was used for each dataset, and the extrapolated average daily temperature swing calculated at the surface. This extrapolated surface value divided by the observed average at 3-in depth gives the scaling multiplier applied to the 3-in temperature record. The scaled 3-in record is then used as a thermal upper boundary condition for the Hydrus 2D heat modeling.

The Hydrus 2D modeling characterized the hydraulic and thermal flow parameters of the sand and the ammonium nitrate pellets. However, the 2D modeling fell short with its inability to calculate surface temperatures, the variable of highest interest to this work. Surface temperature was not measured directly in the EcoCELL, so to successfully simulate subsurface temperature changes, the thermal UBC had to be specified as the adapted version of the Sensor 1 temperature record. Hydrus 1D allows for an energy balance boundary condition, so it was used to run additional endmember scenarios to qualitatively assess the effect of a target on surface temperature.

Hydrus 1D Modeling – Static VWC Models

Four Hydrus 1D models were generated using the EcoCELL medium sand parameterized using Hydrus 2D. Two models included Target A (with the same vertical dimensions), and two had only sand. For each condition, with or without target, one model had VWC fixed at 6%, and the other had VWC fixed at 36.4% VWC. To prevent soil drainage the hydraulic conductivity of the sand was also reduced to 1×10^{-15} cm/hr. This allowed for surface evaporation, but not infiltration. Aside from these variations, all four models were identical. With fixed water contents, these models were not designed to capture the true timing of infiltration around a buried object. Instead, the models simulate endmember soil moisture levels. By applying a range of natural conditions at the upper boundary, we were able to model the range of surface temperature responses for the specified volumetric water contents. The two models without Target A were added to capture some of 2D models' spatial variability (Figures 3, 25), and to test the relative thermal influence of Target A in wet and dry conditions.

Because the enclosed EcoCELLs do not capture the full range of environmental variability, meteorological data were taken from the MERS stationed at YPG in Arizona. Though the station collects discrete reading of incoming and outgoing, shortwave and longwave radiation, these were combined as net radiation for model input. Air temperature, relative humidity, and windspeed were also included from the YPG MERS. Measured surface temperature beneath the station provided a useful ground truth for assessing general modeled performance. Each model ran for 1000 hours, using data collected from 3/14/2019 to 4/25/2019. Input meteorological data is plotted in Figure 13.

The static 1D models are 165 cm deep, with the calibrated thermal parameters for each material. The hydraulic boundary conditions were set as *Atmospheric* above and *Free Drainage* below. Thermal boundaries were set to *Heat Flux* above and *Zero Gradient* below. These models were generated with a one minute timestep to ensure high resolution when comparing the times of day when maximum and minimum temperatures occur.
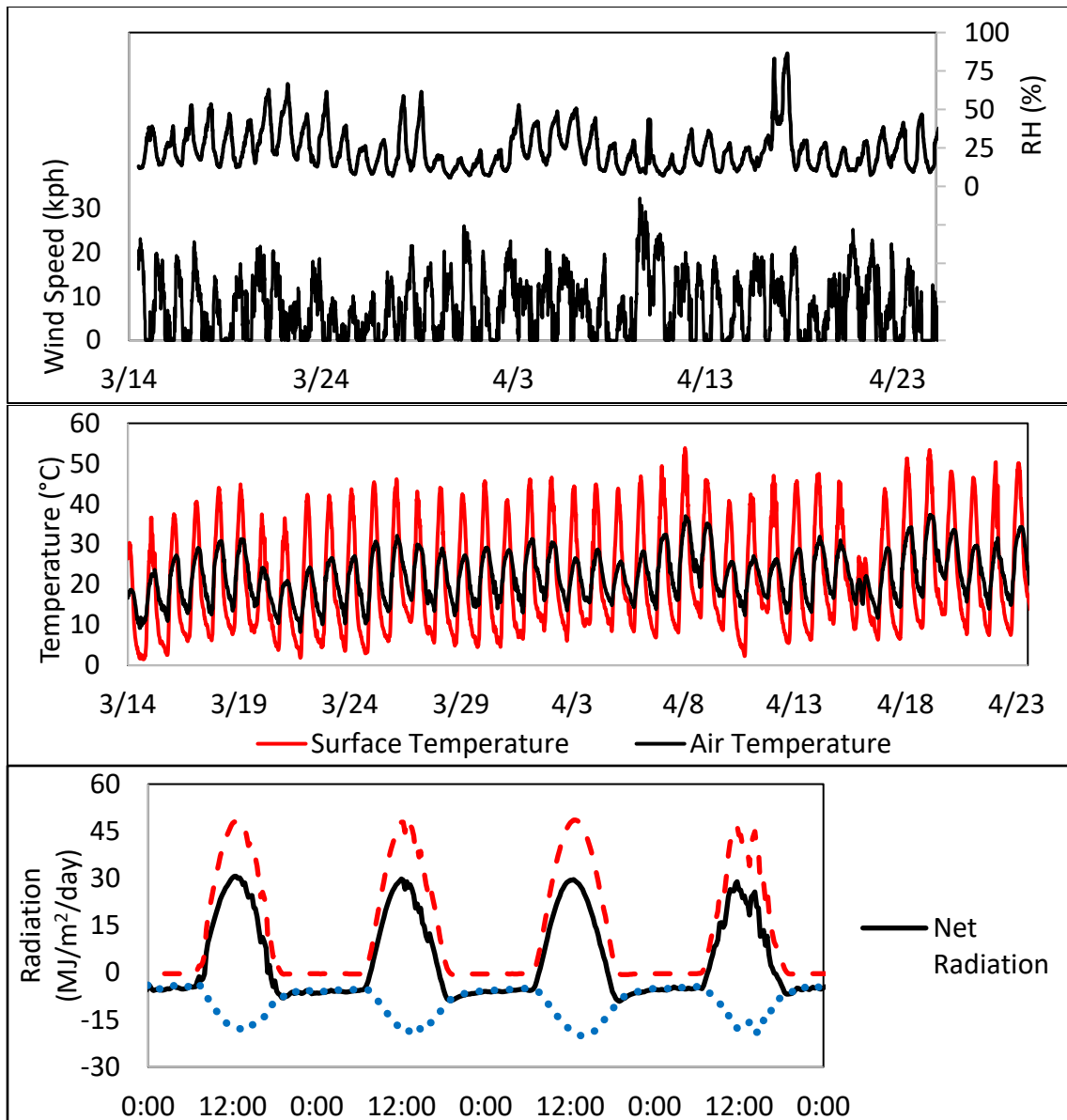
Figure 13: Meteorological data measured at the YPG MERS station, used with Hydrus 1D to estimate surface temperature. The top plot shows relative humidity and wind speed. The middle plot shows air temperature and ground temperature measured below the station. The bottom plot shows a four day sample of measured radiation. SWNET is net shortwave radiation, and LWNET is net longwave radiation.

Results

This section first covers the modeling results for the Hydrus 2D optimization of water flow and heat transport parameters of the EcoCELL sand. Next, the results of the Hydrus 1D fixed soil moisture models are presented.

2D Modeling

The model was successful in representing the impermeable target in the center of the model domain with discrete physical properties from the surrounding soil. Optimized Van Genuchten hydraulic parameters and Chung & Horton thermal parameters are presented in Table 5. Statistical metrics used to assess the model fit to observed data are presented in Table 6. The HYPROP results for the EcoCELL sand indicated residual water content of 6.6%, saturated water content of 36.5%, α of 0.0427, n of 8.570 (very high for n), and saturated hydraulic conductivity of 1.06 cm/day. The HYPROP is not designed to reasonably estimate the high hydraulic conductivities of sand, so the Hydrus catalog value for sand (29.7 cm/hr) was used as an initial estimate and conductivity was inversely parameterized. Residual water content of 6.6% was also not used since the data record shows water contents below that, closer to 5%. The Hydrus catalog sand residual water content of 4.5% was used as an initial estimate. The HYPROP estimate of 36.5% for saturated water content was matched separately in the lab when constraining the Chung and Horton B-parameter for thermal conductivity.

Van Genuchten Hydraulic Flow Parameters					
Material	K_s (cm/hr)	Θ_r [L^3/L^3]	Θ_s [L^3/L^3]	α [1/L]	n
Sand	374.9	0.04331	0.365	0.02891	2.184
Ammonium Nitrate	1E-15	0.01	0.43	1.45	2.68
Chung & Horton Thermal Conductivity Parameters + Vol. Heat Capacity					
Material	λ (b1) ($W^1m^{-1}K^{-1}$)	b2 ($W^1m^{-1}K^{-1}$)	b3 ($W^1m^{-1}K^{-1}$)	C_V ($MJ^1m^{-3}K^{-1}$)	κ (mm^2s^{-1})
Sand - dry	0.229	-1.5	3.1	1.183	0.191
Sand - saturated	Saturated λ measured as 1.6 $W^1m^{-1}K^{-1}$			2.462	0.651
Ammonium Nitrate	0.174	0	0	1.792	0.097

Table 5: Final model parameters for sand and Ammonium Nitrate pellets, measured directly in the lab or inversely optimized using Hydrus 2D. Values for saturated sand were not used for modeling, but are included for reference.

Water Flow Parameter Calibration						
Sensor ID	Depth/Offset [cm]	ME [m³m⁻³]	MAE [m³m⁻³]	RMSE [m³m⁻³]	RMSE-|ME| [m³m⁻³]	RSQUARE
1	7.6, 0	-0.00969	0.01265	0.01751	0.00782	
2	48.3, 0	0.00052	0.00479	0.00831	0.00779	
3	73.7, 0	-0.00305	0.01236	0.01516	0.01210	
5	30.5, 43.2	0.00671	0.00994	0.01426	0.00756	
7	30.5, -33.0	0.00326	0.00813	0.01352	0.01027	
All Sensors - Hydrus Output		0.00061	0.00896	0.01341	0.01281	0.84791
Water Flow Parameter Validation						
Sensor ID	Depth/Offset [cm]	ME [m³m⁻³]	MAE [m³m⁻³]	RMSE [m³m⁻³]	RMSE-|ME| [m³m⁻³]	RSQUARE
1	7.6, 0	-0.01060	0.01229	0.01765	0.00705	
2	48.3, 0	0.00011	0.00630	0.01009	0.00997	
3	73.7, 0	-0.00381	0.01200	0.01546	0.01165	
5	30.5, 43.2	0.00766	0.01273	0.01739	0.00973	
6	30.5, -17.8	0.00015	0.00071	0.00087	0.00072	
7	30.5, -33.0	0.00374	0.00946	0.01428	0.01054	
All Sensors - Hydrus Output		0.00008	0.01007	0.01472	0.01464	0.80910
Dry Heat Transport Parameter Calibration						
Sensor ID	Depth/Offset [cm]	ME °C	MAE °C	RMSE °C	RMSE-|ME| °C	RSQUARE
1	7.6, 0	*Used for Upper Heat Boundary Condition*				
2	48.3, 0	-0.54093	0.54410	0.56679	0.02587	
3	73.7, 0	-0.93300	0.93300	0.94531	0.01231	
5	30.5, 43.2	-1.23057	1.23057	1.32512	0.09455	
6	30.5, -17.8	-0.77608	0.77648	0.87498	0.09890	
7	30.5, -33.0	-0.91585	0.91612	1.02291	0.10707	
All Sensors - Hydrus Output		-0.72170	0.82560	0.93540	0.21370	0.90842
Dry Heat Transport Parameter Validation						
Sensor ID	Depth/Offset [cm]	ME °C	MAE °C	RMSE °C	RMSE-|ME| °C	RSQUARE
1	7.6, 0	*Used for Upper Heat Boundary Condition*				
2	48.3, 0	-0.50003	0.50004	0.61639	0.11636	
3	73.7, 0	-0.77193	1.38283	1.45527	0.68335	
5	30.5, 43.2	-0.99391	0.99391	1.11144	0.11752	
6	30.5, -17.8	-0.70413	0.70448	0.80328	0.09915	
7	30.5, -33.0	-0.74852	0.74870	0.85805	0.10953	
All Sensors - Hydrus Output		-0.62530	0.87850	1.01500	0.38970	0.94159

Table 6: Sensor fit statistics for Hydrus 2D calibration and validation of flow parameters. Sensor 4 (at 139.7 cm depth) is omitted from calibration and validation for lack of data.

Model residuals for the water flow model are presented in Figure 14. Most residuals are less than 0.05 m^3m^{-3} VWC, and overall RMSE is 0.01341 m^3m^{-3} for the calibration dataset and 0.01472 m^3m^{-3} for the validation dataset (Table 6).

Residuals for the dry thermal transport model are presented in Figure 15. There is a persistent positive bias (predicted values > observed values) of about 1°C. The 5TE sensors measure temperature with an accuracy of ±1°C (Decagon Devices 2010). The RMSE of the heat transport calibration is 0.93540°C, while the RMSE of the heat transport validation is 1.01500°C.

Model residuals for the wet thermal transport model are shown in Figure 16, and fit statistics are presented in Table 7. The section from about 2500 hours to 4000 model hours is the Hot/Wet controlled climate test, where the thermal UBC is a scaled copy of the Sensor 1 temperature record. The thermal LBC for this time was fixed at 21°C, and there is a general negative model bias (predicted < observed) of about 1°C. For the Cold/Wet climate test, there is no systematic bias. The wet thermal model validation residuals are within a range of ±1°C, though residuals associated with Sensor 7 consistently peak as high as 5°C (Figure 16). Sensor 7 is at 30.5 cm depth and 33.0 cm away from Target A, though thermal effects from the edge of the soil plot are assumed to be negligible. The RMSE for the full wet thermal transport model validation is 1.015°C, above sensor accuracy.

The hydraulic model successfully simulated the retention and infiltration of water above and around Target A (Figure 17). These results show that even for a sand with high hydraulic conductivity there is a disruption to water flow caused by an impermeable object.
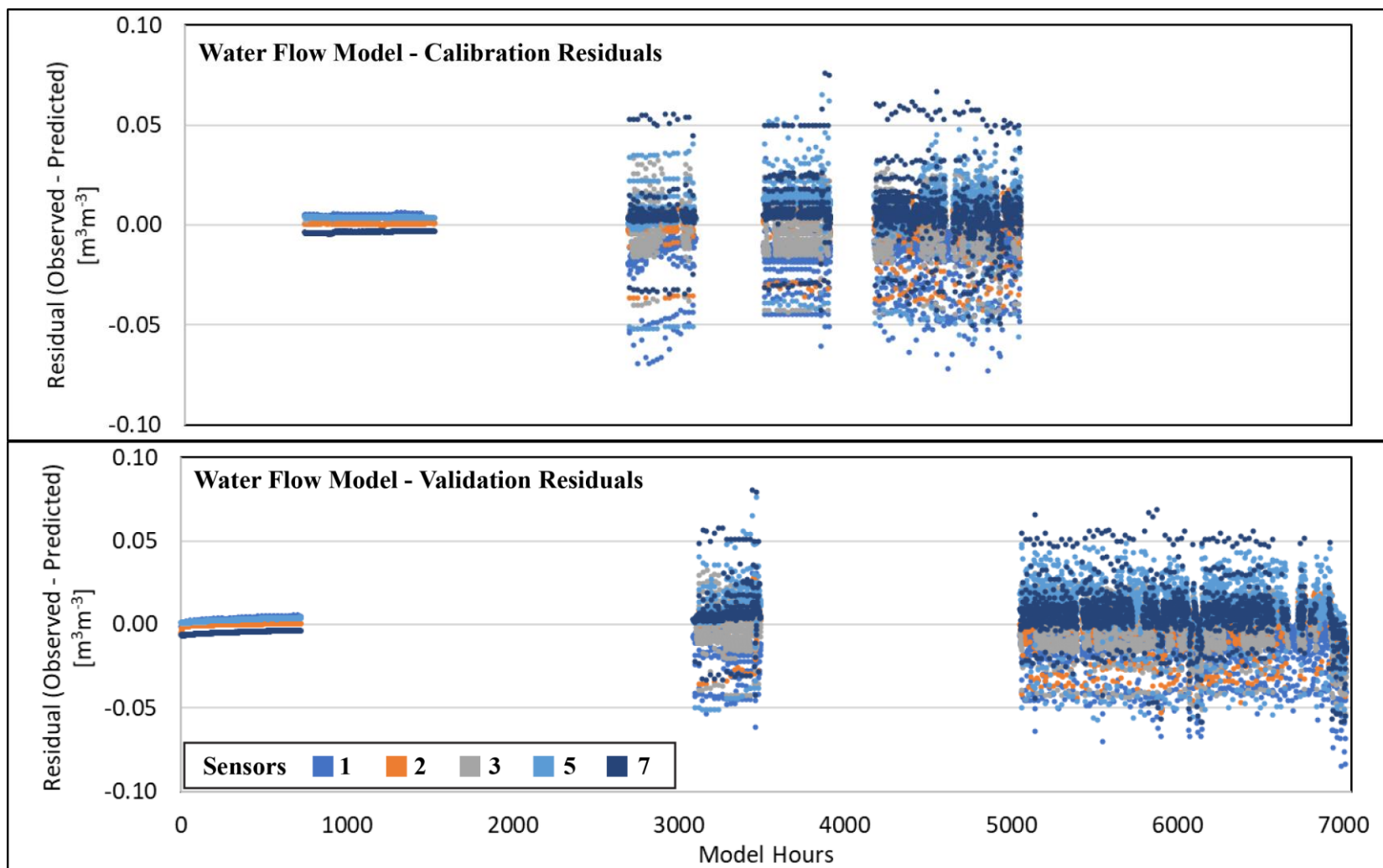
Figure 14: Residual fit results for the Hydrus 2D water flow parameterization model.
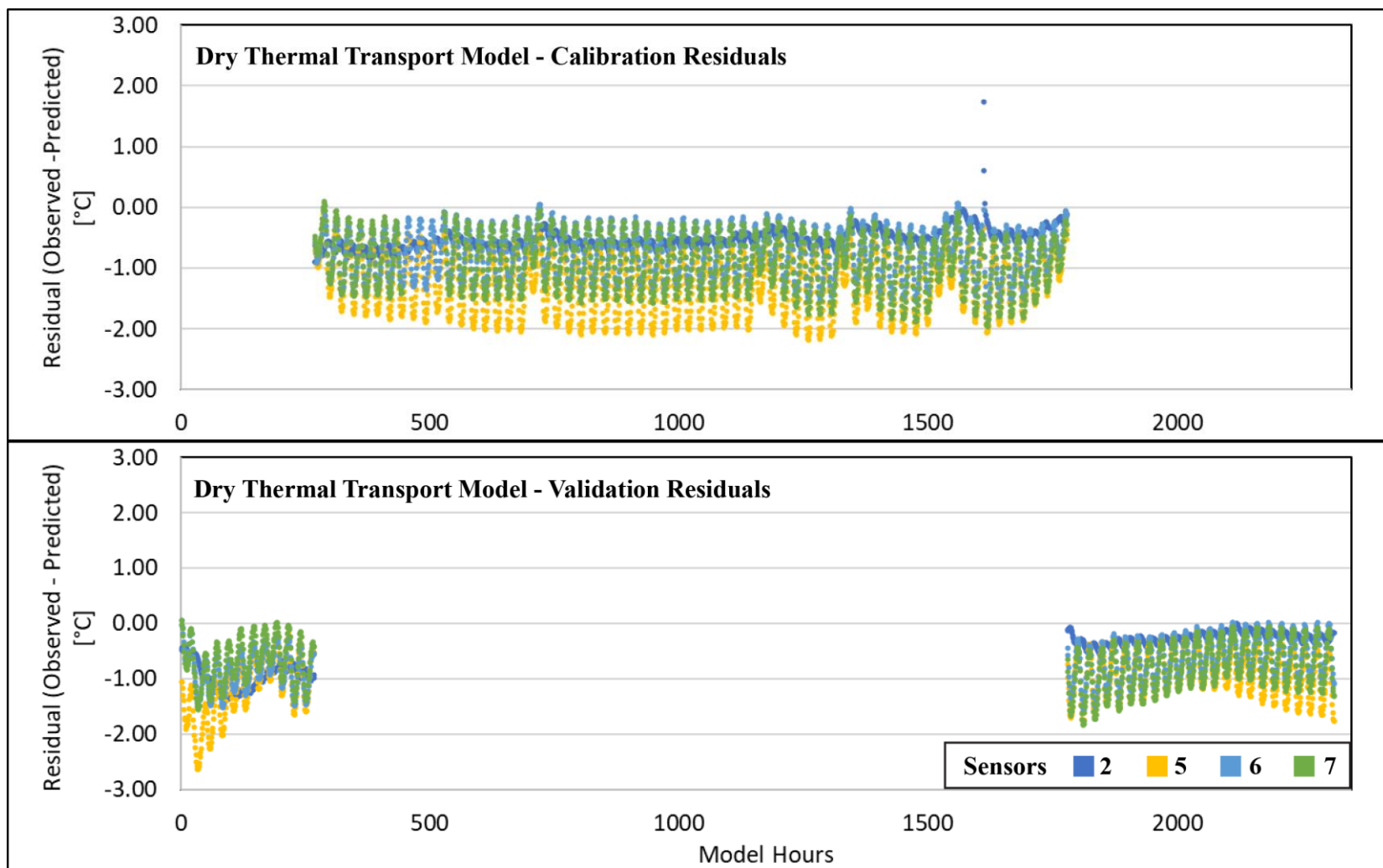
Figure 15: Residual fit results for the Hydrus 2D heat transport parameterization model.
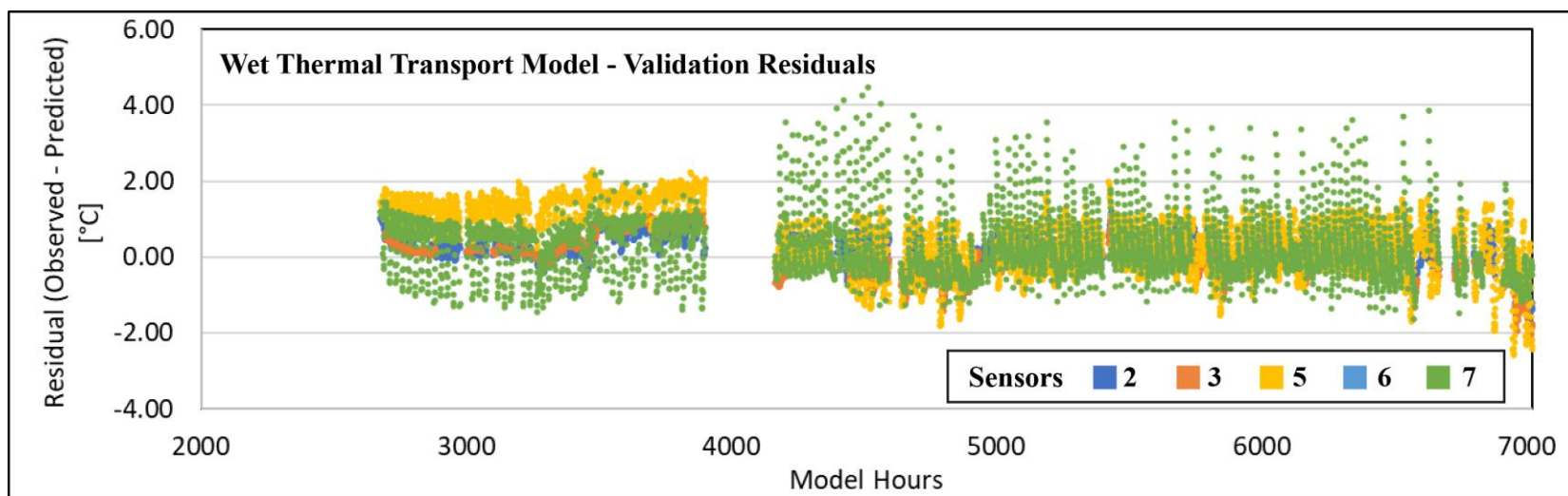
Figure 16: Residual fit results for the wet thermal model using heat transport parameters that were optimized using only the dry portion of the experimental data. Note the omission of the first sensor, as its record was modified for used as an upper boundary condition. The gap around 4000 hours is the transition from Hot/Wet to Cold/Wet conditions.

Wet Thermal Model Validation						
Obs Node	Depth/Offset	ME	MAE	RMSE	RMSE-|ME|	RSQUARE
1	7.62, 0	*Used for Upper Heat Boundary Condition*				
2	48.26, 0	0.50873	0.53396	0.60959	0.10086	
3	73.66, 0	0.45480	0.50591	0.59406	0.13926	
5	30.48, 43.18	0.48521	0.58143	0.70103	0.21582	
6	30.48, -17.78	0.47584	0.67080	0.86238	0.38654	
All - Hydrus Output		0.48148	0.57404	0.70510	0.22362	0.99313

Table 7: Sensor fit statistics for Hydrus 2D validation of dry-calibrated heat transport parameters. Sensor 4 is omitted.
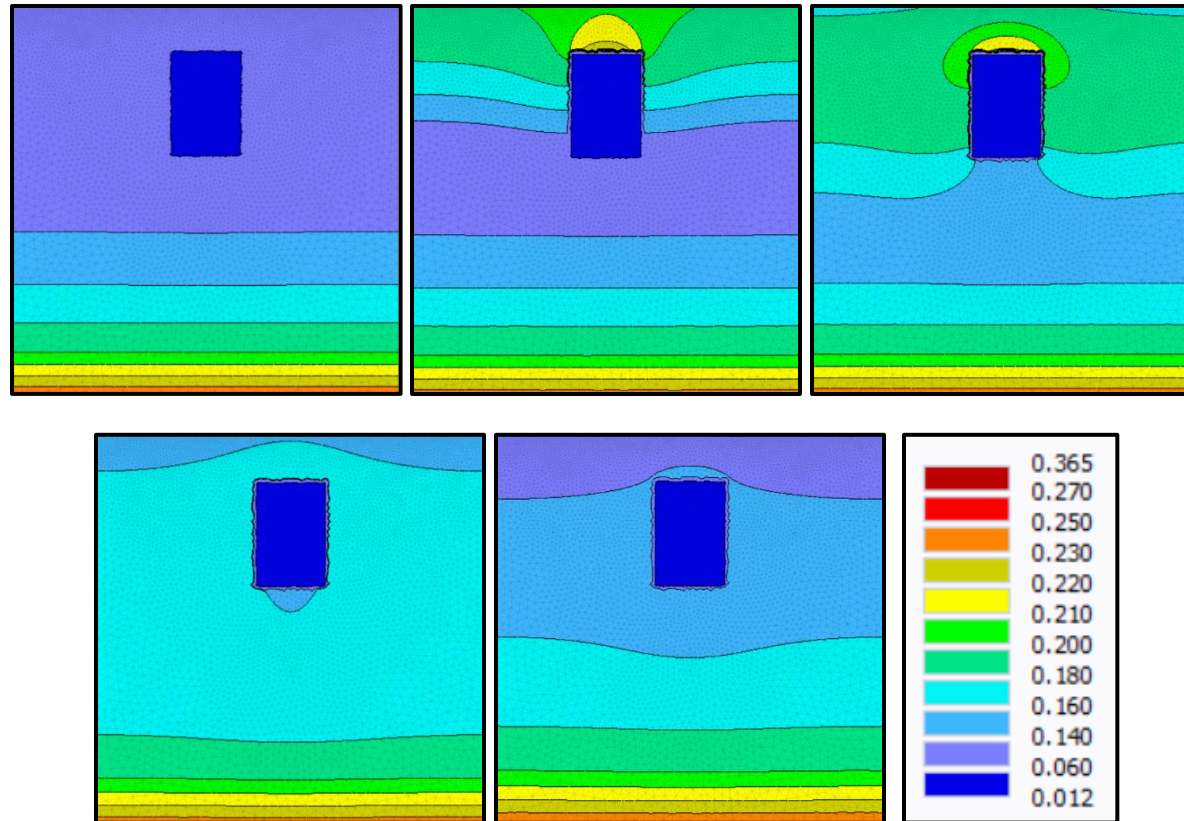
Figure 17: Water content distributions surrounding Target A during a 30 minute watering pulse. Top-left shows just before watering, and depicts the static soil water content between watering pulses. Top-middle shows 15 minutes time, with a peak difference between water contents above and adjacent to Target A. Top-right shows 30 minutes time, immediately after watering has stopped. Bottom-left shows 45 minutes time, when the relative increase in soil water ponded over Target A has decreased significantly. Bottom-right shows 90 minutes time, when water contents are beginning to resemble static conditions. Each color band represents a range of volumetric water contents in m^3m^{-3}. This scaling i non-linear to accentuate the patterns of flow around Target A.

1D Modeling

Measured ground temperature is called "Proxy Surface Temperature" in Figure 18, which shows the soil and air temperatures for all four models. The models that include Target A are called "Center", and those without are called "Side."
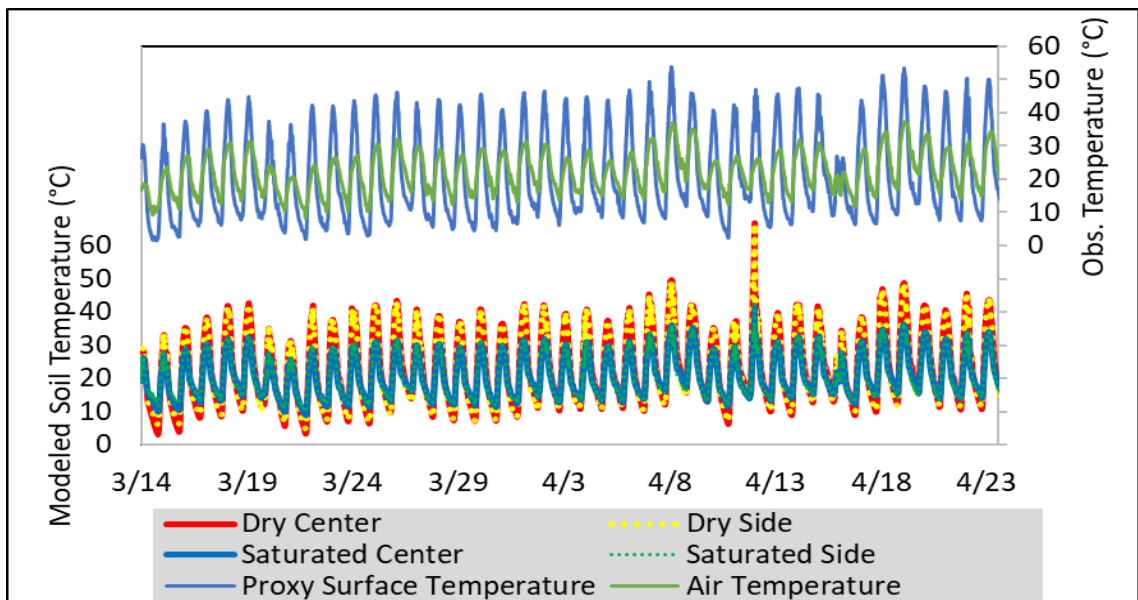
Figure 18: Comparison between air temperature and ground temperature measured at the YPG MERS station in Yuma, AZ (top) and soil surface temperatures modeled using Hydrus 1D (bottom).

Surface energy balance output for the four 1D models is shown in Figure 19, comparing shortwave, longwave, and total net radiation (Panel A), plus latent, sensible, and ground heat fluxes (Panels B-D). Ground heat flux is approximately equal for all models.

Figure 20A shows a comparison of daily maximum and minimum temperatures for the Center models. The same comparison between the Side models is shown in Figure 20B. The saturated models have lower maximum temperatures and higher minimum temperatures compared to the dry models. A similar comparison to Figure 20 is presented

in Figure 21, but the panels are separated by water content rather than by the presence of Target A. For the saturated models, both the maximum and minimum daily temperatures are roughly 3°C higher on average with the target than without (Figure 21A). For the dry models, there is negligible difference in maximum or minimum surface temperature with or without the target (Figure 21B).

Figure 22 shows another comparison of peak and trough daily temperatures, between the saturated Center model and the dry Side model. This plot shows the effect of Target A in an exaggerated sense, as though the soil adjacent Target A has dried completely, but there remained maximum perched soil water above Target A. Average maximum daily temperature is approximately 5°C lower for the saturated Center model, and average minimum daily temperature is approximately 7°C higher.

Box and whisker plots are presented in Figure 23 showing the distributions of when maximum and minimum daily temperatures occurred for each model. For this modeling, changing peak times do not follow a trend one would expect to see over a longer, seasonal timeframe, as daylight hours change. For this reason, I compared the overall distributions of peak temperature timing. Maximum daily temperatures occur earlier under dry conditions than under saturated conditions by approximately 30 minutes. There is also a larger variance of dry maximum temperature times compared to saturated maximum times. For minimum daily temperatures, there is negligible difference in timing between and of the four models. Median minimum daily temperatures are equal for all models except for the saturated Side model, which occur 15 minutes earlier. The average minimum daily temperatures all occur within 15 minutes of each other. Table 8 lists the average peak temperature times for each model.
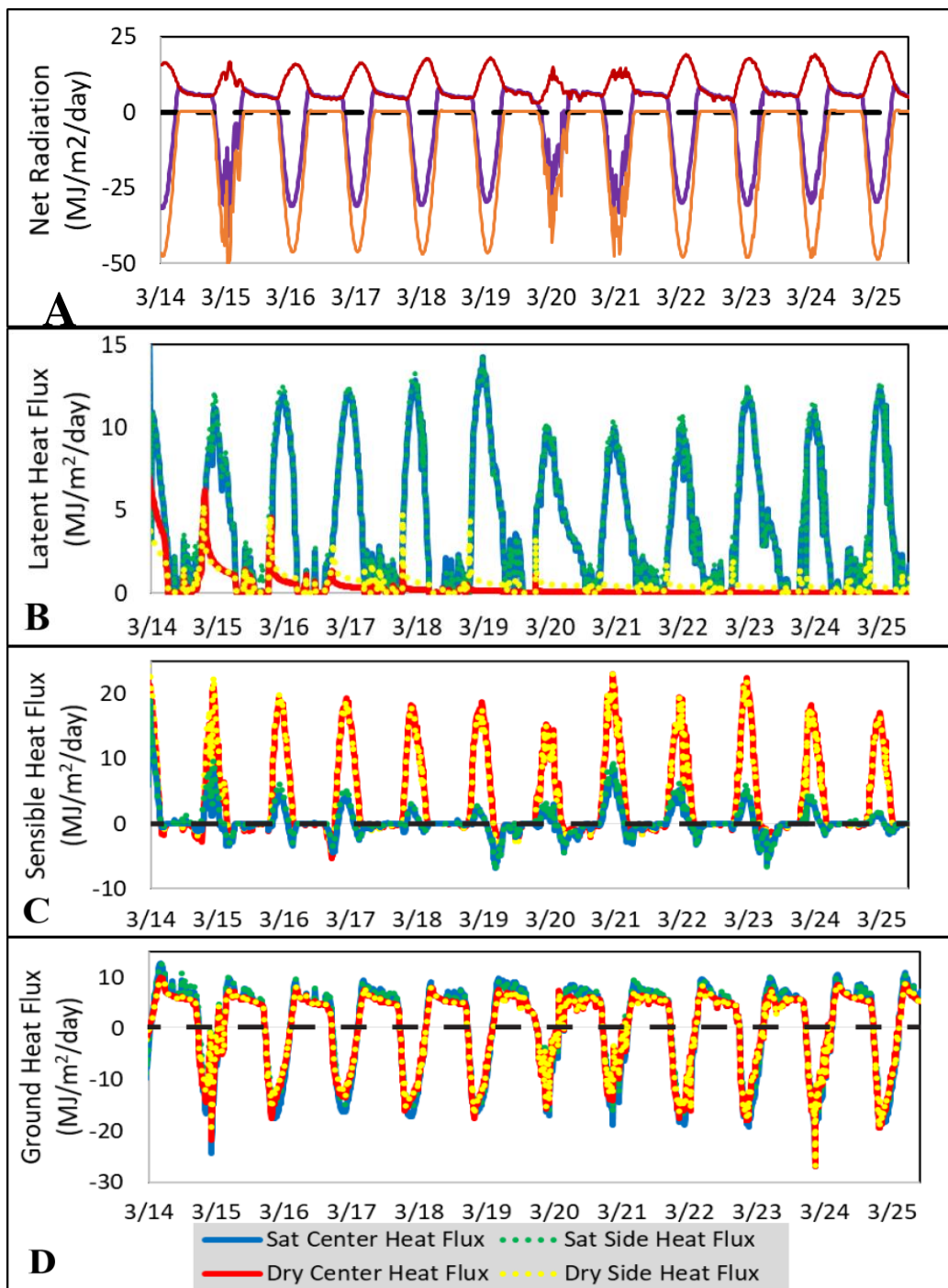
Figure 19: Output surface energy components for the 1D models. Panel A shows net shortwave radiation (orange), net longwave radiation (dark red), and net radiation (purple), which is exactly equal to input net radiation. Panel B shows latent heat flux, Panel C shows sensible heat flux, and Panel D shows ground heat flux, all calculated by Hydrus. All fluxes are positive outward.
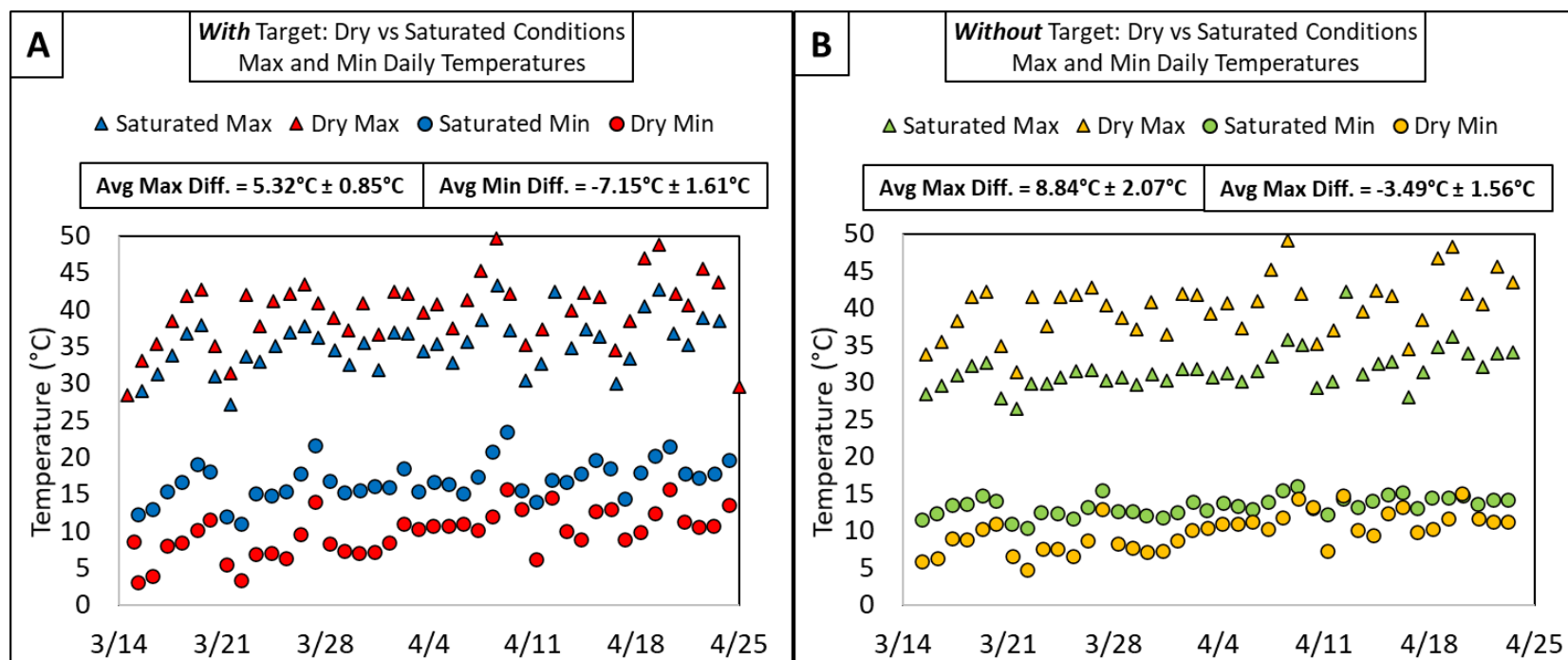
Figure 20: Comparisons of maximum and minimum daily soil surface temperatures between saturated and dry conditions. Panel A compares the two models with Target A, and Panel B compares the two without Target A. Maximum temperatures are triangles, and minimum temperatures are circles. The average (and standard deviation) difference between maximum and minimum values (Dry minus Wet) is listed immediately above each plot.
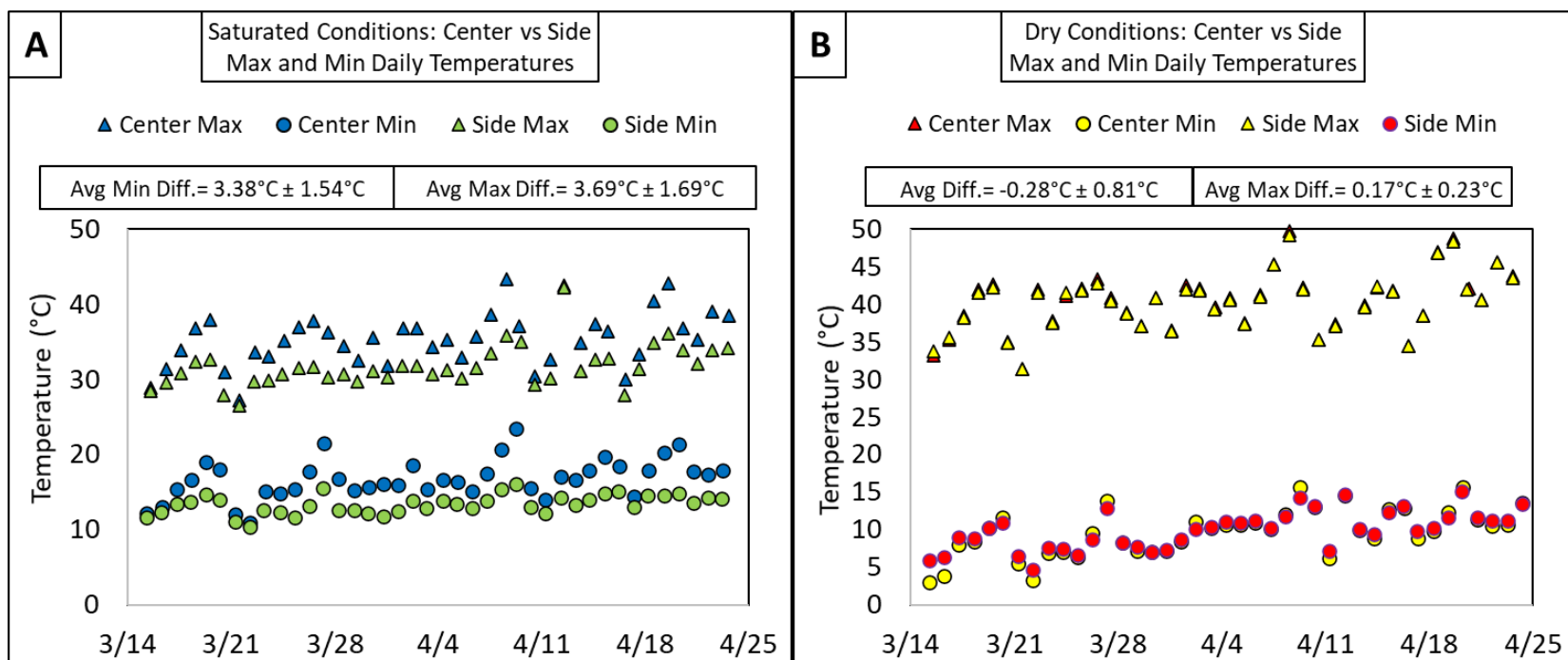
Figure 21: Comparisons of maximum and minimum daily soil surface temperatures between Center and Side models, or those with Target A compared to those without. Panel A compares the two models with saturated conditions, and Panel B compares the two models with dry conditions. Maximum temperatures are triangles, and minimum temperatures are circles. The averages and standard deviations for these differences (Dry minus Wet) is listed immediately above each plot.
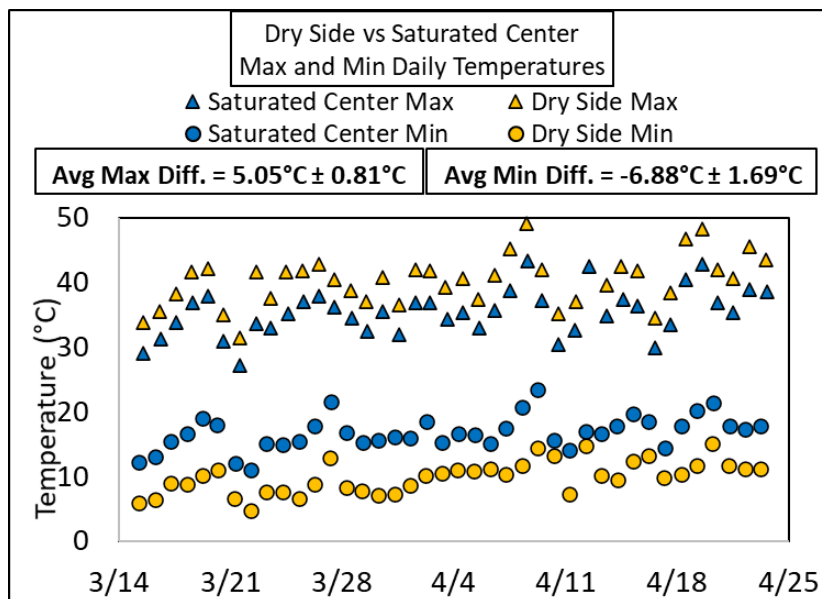
Figure 22: Comparison of the Saturated Center model and the Dry Side model maximum and minimum daily soil surface temperatures.
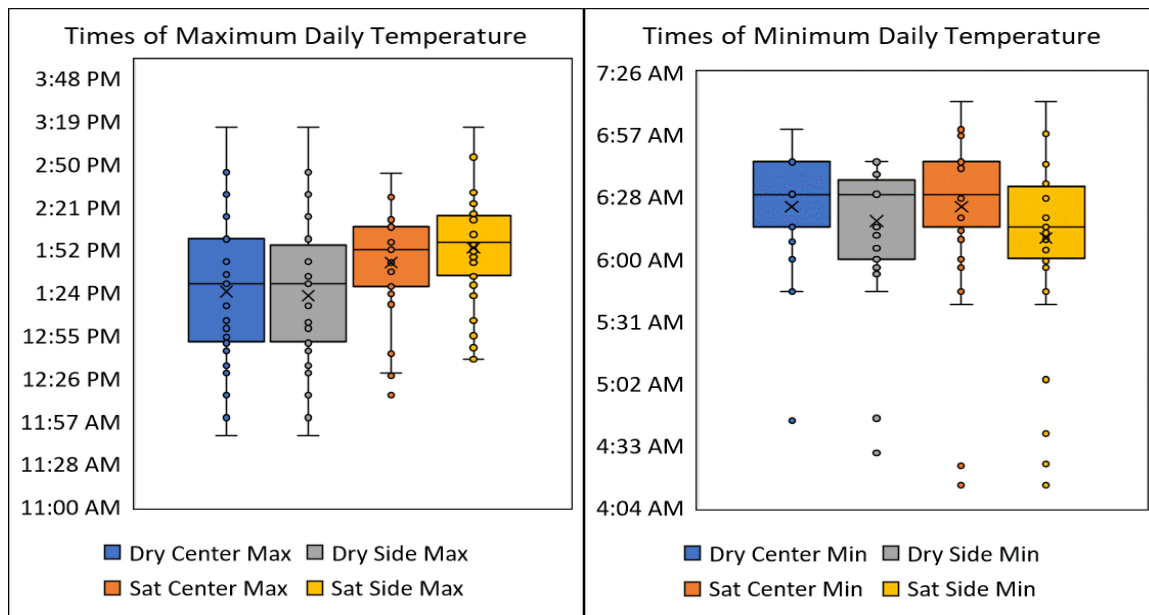
Figure 23: Box and whisker plots indicating the timing of maximum and minimum surface thermal temperatures for each of the four Hydrus 1D models. Median times are the middle line through each box, and "X" marks the average time.

Model	Condition	Value	Time (Average + Standard Deviation)
Center	Dry	Maximum	13:24 ± 56 min
Center	Saturated	Maximum	13:44 ± 51 min
Side	Dry	Maximum	13:22 ± 61 min
Side	Saturated	Maximum	13:54 ± 41 min
Center	Dry	Minimum	6:24 ± 25 min
Center	Saturated	Minimum	6:24 ± 33 min
Side	Dry	Minimum	6:17 ± 34 min
Side	Saturated	Minimum	6:09 ± 49 min

Table 8: Daily average maximum and minimum temperatures for the four Hydrus 1D models.

Discussion

2D Water Flow

The Hydrus 2D modeling constrained flow parameters and generated a reasonably calibrated simulation of the EcoCELL sand. The 2D models also demonstrate that a buried object can be incorporated into the model domain such that it is impervious to water flow, but allows for heat transport. The 2D modeling was also useful in capturing and visualizing the dynamics of heat and water flow changes associated with a buried object. However, Hydrus 2D has a limited capability to model surface processes for the purposes of this study. The two options for a thermal UBC in Hydrus 2D do not allow for calculation of surface temperature, and there is no way to specify energy balance. Surface temperature and incoming water temperature were not measured directly, though even if they had been, there is still no way to account for surface heat fluxes using Hydrus 2D. In addition to these limitations, several other assumptions were made during the 2D modeling for both hydraulic flow and thermal transport parameterization.

Incorporating a buried target into the Hydrus model is imperfect, but possible. The challenge is that boundary conditions can only be specified along the outside edge of the model domain. Hydrus allows for holes to be cut through surfaces, which can have boundary conditions (useful for simulating drains), but only if that area is open. Target A cannot be modeled simply as an opening in the sand with zero-flux boundaries because the thermal properties of the target affect the heat flow in the surrounding soil. Additionally, Target A has a plastic shell that is impervious to water, but which allows for heat exchange. Setting the K_s of the ammonium nitrate to 1×10^{-15} cm/hr does not exactly replicate a no-flow water boundary, but it is a realistic approximation. No water flow into or within the target was observed.

Estimated water flow parameters from the Hydrus 2D models are reasonable for the sand (Table 5). Saturated water content was measured directly as 0.365 m^3m^{-3}, and the estimate of residual water content taken from the data was close to the final value of 0.043 m^3m^{-3}. The other inversely parameterized Van Genuchten variables are also reasonable estimates for a sand. The calibrated K_s of 374.9 cm/hr is above most upper estimates for medium sand, but well below the maximum K_s for coarse sand (Duffield 2019). The uniformity of the Quikrete medium sand used may account for the higher K_s than natural sands.

Figure 14 shows the model residuals for the calibration and validation of the 2D water model, with many residuals peaking around 0.05 m^3m^{-3}, above the sensor accuracy of 0.02 m^3m^{-3}. These errors correspond to the twice daily watering times when soil moisture was highest, indicating the model fails to match the magnitude of peak water fluxes. The high hydraulic conductivity of the sand and rapid resultant infiltration meant

the soil dried out between each watering, thus each watering imposed a steep hydraulic gradient in VWC and matric potential. The timing of these fluxes is captured, and an overall RMSE of 0.013 m^3m^{-3} is within sensor accuracy.

2D Heat Flow

Hydrus 2D is less functional with regards to energy balance than the 1D version. Surface temperature cannot be inferred in Hydrus 2D by specifying meteorological variables. Internal soil heat transport was modeled using Hydrus 2D, but several issues arose throughout the process.

Hydrus requires agreement between heat and water boundaries, meaning a zero-flux water flow boundary must be a zero-flux heat transport boundary (Šimůnek 2006). The sides of the EcoCELLs are insulated with 13 cm of concrete surrounded by 40 cm of foam that extends down fully along the sides, so it is reasonable to assign a zero-flux condition to the sides of the model. The boundary between sand and OK soil (separated by a plastic sheet) is not represented in the Hydrus model, so neither are any thermal effects of the adjacent OK soil, but the boundaries for the plane of sensors are represented. The deepest sensors for the OK soil plots showed slightly increased daily thermal variability compared to sensors nearer the center of the soil columns. This indicates some diurnal thermal fluctuation along the bottom of each plot, meaning assigning a zero-flux heat LBC is not strictly correct.

Hydrus 2D allows for two types of thermal boundary conditions. Type 1 is a specified value boundary condition, and Type 3 is a flux type boundary condition, which ascribes the specified temperature to water fluxes into the domain (Šimůnek 2006). A Type 3 heat boundary is more physically realistic since it preserves heat mass (Van Genuchten

1984, Leij 1991). However, for the Type 3 heat boundary condition, Hydrus assumes that if there is no water flux, no heat flux occurs no water flux means no heat flux because the specified temperature is ascribed only to inflowing water (Šimůnek 2017). Since water temperature was not measured and dry conditions were used to determine conductive heat transfers within the soil, the specified temperature Type 1 boundary was the only option. What is needed for this research is a Type 2 boundary that allows for specified time-varying surface energy flux based on environmental data.

Four options for thermal UBC were tested in Hydrus 2D: A Type 1 UBC with observed air temperatures, a Type 1 UBC with simulated air temperatures, a Type 3 UBC with fixed water temperature, and a Type 1 UBC adapted from the shallowest observed soil temperatures, the last of which provided the best model fit. This last option benefits from using observed soil data from Sensor 1, which responded both to fluctuations in air temperature and to changes in heat advected by infiltrating water. However, the Sensor 1 record has numerous gaps in coverage, its use as an UBC excludes it from model calibration, and there is not enough data to have reliably scaled the record based on daily temperature amplitudes.

The method used to fill the Sensor 1 data gaps is more accurate than a simple linear fill since it approximates the diurnal variations observed in the EcoCELL, however it requires a few assumptions. Filled daily maximum and minimum temperatures were fixed at 15:00 and 03:00, respectively, though the true timing of peak temperatures varies in the record. Another problem is that the baseline linear fill does not account for when the record breaks. Interpolating from a high value to a distant low value adds a slightly higher gradient

to the linear fill. Despite the inaccuracies with sinusoidally filling data gaps, this method is the best choice available without another means of approximating the missing data.

Stallman (1965) provides equations to estimate percolation velocity from the attenuation of diurnal signal with depth through the soil column, assuming only vertical conductive heat transport. Using this method is the best option available for projecting surface temperature based on subsurface temperatures, but there is not enough near surface vertical sensor density to support it. For the Hot/Dry experiment, the average daily range of Sensor 1 temperature is 6.54°C, and the average range for the 30.5 cm depth sensors (Sensors 5, 6, and 7) is 0.4°C (Figure 12). 5TE sensor resolution is 0.1°C, so the average temperature range for the 30.5 cm depth sensors is greater than the maximum expected error of 0.2°C. However, the diurnal signal extinguishes very rapidly, and two reliable data points is not enough to reasonably constrain an exponential regression. The Hot/Wet and Cold/Wet experiments show clearer diurnal signals for Sensors 5, 6, and 7. Some authors suggest that diurnal temperature signatures typically penetrate the upper 15 cm, in the vicinity of typical mine burial (Smits 2013, Garcia-Padron 2002, Šimůnek 2001). Sensor 1 is best suited for this meteorologically-dependent scaling approach, and more sensors concentrated near the soil surface would likely improve model fit. It would also be preferable to have a near surface sensor to the side of Target A for direct comparison of measurements.

Sensor 1 data were excluded from the heat model calibration and validation to avoid direct bias with model results. Without the Sensor 1 record there are too few near surface sensors to reasonably assess model performance in terms of heat transport. There is also no means by which to verify the accuracy of the scaling method since there is not a single

point measurement of surface temperature. Furthermore, Sensor 1 is a solitary point, and that single record was applied across the entire 2D upper boundary. Since Sensor 1 is centrally placed above the target, any effects of Target A's presence are applied across the top of the model domain. When the Sensor 1 record was extended for the Hot/Wet and Cold/Wet experiments to validate thermal transport parameters under wet conditions, this bias toward a central sensor was again applied across the entire UBC. Sensor A temperatures that are altered by water ponding above Target A are assumed to apply across the entire model domain.

Hydrus 2D was used to effectively capture the water flow around Target A, but there is no way to assess the corresponding heat flow. Chung and Horton b-parameters for correlating water content to thermal conductivity were constrained directly, but with the uncertainty in thermal boundary conditions, it is impossible to claim that the 2D heat model correctly represents heat flow through the sand. The proxy surface temperatures extrapolated from the Sensor 1 record apply to a single point of a complex system, and there is no way to confirm the accuracy of the scaling method.

Predicted temperatures show a consistent bias of about 1°C above observed temperatures (Figure 15). This offset is likely due to an error with the scaling factor applied to the Sensor 1 record. Changes to the thermal LBC had minimal effect on model fit. As with the water model residuals, there are regular deviations from observed values, however, for the heat model these variations correspond to daily maximum and minimum temperatures, not to watering times (Figure 15). There is no apparent drift in the modeled data, meaning model residuals do not become progressively higher or lower, but the periodic cycle in the residuals indicates poor simulation of heat transport. The excursions

from observed values are most pronounced for Sensors 5, 6, and 7, the shallowest (30.5 cm depth) sensors used for calibration. Sensor 2 beneath Target A is mostly closely matched by the model, but also experiences far smaller diurnal temperature variations (Figure 12). An example of a direct comparison between modeled and observed values is shown in Figure 24, illustrating not only that modeled temperatures are consistently higher than observed, but that they exhibit a more exaggerated response to surface temperature changes than was observed. Sensors 6 and 7 show the same increase in variability, which indicates that the scaling factor of the Sensor 1 record is too high.
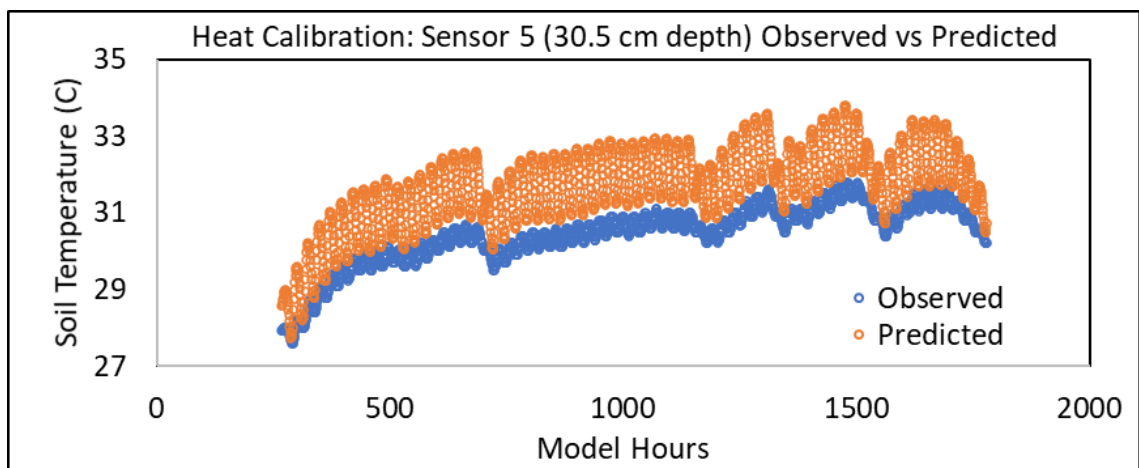
Figure 24: Direct comparison of observed and modeled (predicted) temperatures for Sensor 5, buried at 30.5 cm depth. These calibration results apply to the Hot/Dry EcoCELL test which ran from 5/19/18 to 8/27/18. Sensors 6 and 7 at the same depth differ similarly from modeled values.

The 2D heat model was not calibrated further since there remains the inability to assess the surface processes central to this study. Also, the scaling factor for the Sensor 1 record was derived from the observed data, so manipulating it further to match the data more closely would be improper. The same 1.7x scaled thermal UBC was extended to the

wet experiments next, with results shown in Figure 16. Again, the highest variability in errors is shown by the shallowest sensors, and this variability is most apparent for Sensor 7, which is furthest to the side of Target A (Figure 5). The increased residuals for Sensor 7 most likely stem from the bias incorporated by adapting the Sensor 1 record to a thermal UBC. Water retained over Target A following each watering pulse prolonged temperature changes observed by Sensor 1, relative to Sensor 7 where water infiltrated more rapidly. That Sensor 7 shows increased error relative to sensors closer to the retained moisture indicates there is a spatially variable thermal effect from retained soil moisture.

The wet thermal transport model residuals also show the transition from hot to cold conditions in the EcoCELL. For the Hot/Wet test (model hours 2600-3900), residuals are generally +1-2°C, meaning the model underpredicted temperatures. For the Cold/Wet test (model hours 4165-7020), modeled temperatures more closely match observations, with residuals around ±1°C. The increased errors of the Sensor 7 record shift from negative to positive, meaning the model first tends to overpredict Sensor 7 temperatures, then tends to underpredict them. These peak errors correspond to minimal daily temperature, indicating the Cold/Wet experiment did not get quite as cold at night as was modeled.

Static VWC 1D Models

Without direct measurements of the temperature of the infiltrating water, or of the true surface temperature, there is no way to quantify the relationship between water content and surface temperature using Hydrus 2D. Hydrus 1D allows users to input variables such as humidity, wind speed, cloudiness, and net radiation, and will then estimate evaporation and latent heat exchange (Šimůnek 2005). While Hydrus 1D can infer surface temperatures based on environmental variables, it is unable to replicate water flow down and around

Target A. An example of 2D water flow is depicted in Figure 25, showing increased soil moisture above Target A, and an area of reduced soil moisture below. Figure 25 also illustrates the horizontal components of flow velocities around Target A that cannot be captured by a Hydrus 1D model. To address this problem, I used Hydrus 1D to simulate surface temperatures under several static endmember scenarios. Though the MERS atmospheric data are not artificial, the static water flow imposed in the soil column does not represent truly natural conditions. Rather, the 1D models provide a range of natural responses to two fixed water contents, meant to maximize surface thermal contrast.
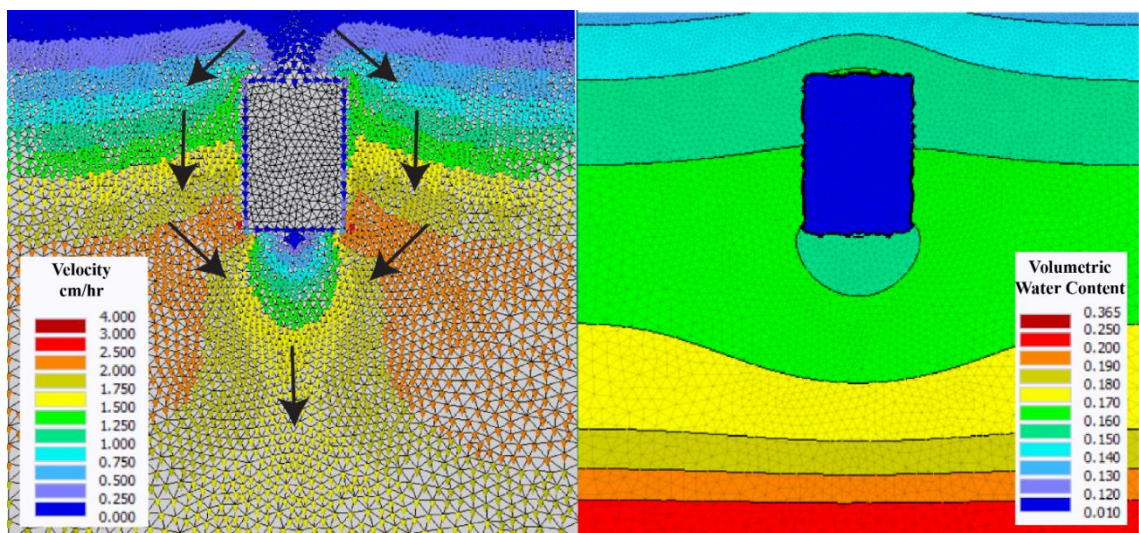
Figure 25: Example distribution of soil water around Target A following watering. The left panel shows nodal water velocities in cm/hr, with higher velocities closer to red. The velocity vectors are too small to see in this image, so larger arrows are added to indicate flow direction. The right panel shows the corresponding volumetric water content distribution, scaled from dry to saturated, 1% to 36.5% VWC, respectively. Note the increased water retention above Target A.

Meteorological data from the MERS station is typical of the arid Yuma, AZ environment, though it is important to note that no precipitation occurred throughout the record used for this modeling. For a more dynamic modeling setup than these static VWC models, simulated soil watering (either natural or artificial) would provide insight into the timing of water retention around a buried object and the effect of antecedent moisture on surface thermal signatures. Otherwise, the input data follows expected trends, with incoming solar radiation during daylight, and outgoing longwave radiation at night (Figure 13). The inclusion of wind speed in the input data allowed for removal of heat at the surface and proper calculation of latent energy flux.

Output meteorological fluxes for the 1D models also followed expected trends (Figure 19). The dry models exhibit higher outward sensible heat flux compared to the wet models, but lower latent heat flux (Figure 19B, 19C). This is consistent with the theory described in the background section, given that more energy in a wet environment will be spent warming and evaporating water, and heat is more easily conducted down through wet soil than through dry soil. Outward latent heat flux persisted throughout both saturated tests, though there is no way to confirm whether the estimates are accurate. For the dry models, there is an initial latent heat flux, which diminishes quickly, indicating that the fixed water content of 6% is too high for these dry conditions. The inferred surface temperatures of all four models closely track the surface temperature measured below the MERS station, indicating good model fit. The dry models have an especially strong correlation to the observed surface temperature data, which is expected given that the Yuma soil was also completely dry.

Comparing the magnitude and timing of peak temperatures between the four modeled cases provides some insight into the research questions posed by this study. Under saturated conditions there is a smaller amplitude of daily surface temperature variation compared to dry conditions (Figure 20). More energy is devoted to latent heat exchange under saturated conditions, and the higher volumetric heat capacity of water allows for wet soil to retain more heat while showing less temperature change, thereby damping daily temperature fluctuation.

The Side models *without* Target A, comparing saturated to dry conditions, show a greater difference between maximum temperatures than between minimum temperatures (Figure 20B). During the day, when the primary energetic flux is incoming solar radiation, soil moisture plays a relatively greater role in absorbing incoming energy than it does at night when much of that energy has been re-radiated, spent as latent energy, or conducted through the soil. This result suggests that increased soil moisture damps maximum daily temperatures more than minimum daily temperatures.

The reverse is true for the Center models *with* Target A, again comparing saturated to dry conditions, where there is a greater difference between minimum temperatures than between maximum temperatures (Figure 20A). Target A thermal conductivity is lower than that of sand, and far lower than saturated sand (Table 5). This lower thermal conductivity mass serves as a barrier to heat transport, meaning heat is retained near the surface for longer and minimum daily temperatures are relatively higher than without Target A, especially under saturated conditions. This result suggests that when Target A is present, saturating the soil has a greater relative impact on temperature signal at night than it does during the day.

Figure 21 frames the same comparison of maximum and minimum temperatures, but based on saturated versus dry conditions. For dry conditions, there is a higher standard deviation than average difference between maximum and minimum temperatures, with or without Target A, indicating no apparent influence of Target A's thermal properties on surface temperature (Figure 21B). This does not rule out the potential role of the thermal properties of Target A on surface temperature. The difference in heat retention of Target A compared to the sand will likely be most apparent between peak temperatures, assuming the different thermal properties of target and soil cause different rates of temperature change.

For saturated conditions, there is a noticeable difference between the Center and Side models (Figure 21A). Both the maximum and minimum temperatures of the Center model are approximately 2-6°C higher than those of the Side model. The 1D models do not account for horizonal or advective heat transfer, so the magnitude of this difference is not reliable, but it does suggest that the presence of an impermeable object influences surface heat flow. With lower thermal diffusivity and conductivity, Target A impedes the vertical transport of a diurnal heat signal, causing more heat to accumulate above the target. For the saturated Side model, there is a greater mass of high κ, high λ material compared to the Center model, so temperatures equilibrate faster, and heat is conducted more readily into the soil.

The greater difference in thermal properties between sand and ammonium nitrate under saturated conditions suggests that shifts in the timing of peak temperatures will be more pronounced for the saturated models. A comparison of the timing of average daily maximum and minimum temperatures is presented in Figure 23. There is no consistent,

observable difference in the timing of the peak and trough daily temperatures between the four columns evaluated. The variance of timing differences outweighs the differences between all 1D models (Table 8). A more sophisticated model, especially one that can account for lateral water and heat transport, is needed to tie the magnitude and timing of temperature changes to changes in water content.

In terms of landmine detection, the 1D modeling results indicate a potential for soil watering to be used as a tool to improve surface thermal contrast. The presence of a near surface object that is impermeable to water flow will pond water near the surface, thereby damping diurnal surface temperature signals relative to unobstructed adjacent soil. This damping effect may be more pronounced at night, when comparing relative minimum daily temperatures, than at maximum daily temperatures. By comparing maximum and minimum daily temperatures, when differing thermal properties of a landmine are relatively less important, these results support the fact that soil watering can improve surface thermal signature regardless of landmine composition. This result is important, as it shows the potential for soil watering to improve the timing constraints of thermal landmine detection.

Model Assumptions

Several assumptions of this modeling should be reviewed when interpreting the results. Bruschini (1997) points out that vegetation, surface roughness, clutter (random buried objects), and soil organics will all complicate thermal detection efforts. The scope of this modeling is also restricted to only one type of soil, with one target type. Variations of target depth, shape, material properties, and soil properties remain widely untested. This modeling was designed to test the capability of the Hydrus software in evaluating surface

temperature response for a single target configuration, to create a template for further comparisons, but these results cannot be assumed universally.

The EcoCELL experiments were conducted using a clean, commercial grade sand, and no organic material was included in the model. Organics may be present when demining is necessary, and should be incorporated into any models intended to account for all potential changes to thermal transport, soil drainage, transpiration of water to the surface, and surface vegetation cover, among other considerations. Whether the presence of soil organics would benefit or hinder landmine detection is beyond the scope of this study, though I suspect that the presence of vegetation cover would impede accurate surface temperature measurements. As a ubiquitous component of most soils, the effects of organic material on surface temperature should be understood for real-world demining applications.

This modeling also assumes a smooth soil surface, though in reality, surface roughness affects soil emissivity and should be considered if incorporating measured surface temperatures into a model. Soil disturbance may be a key factor in determining surface temperature response, one which is not explored by this research. Soil disturbed naturally or during burial will likely have altered hydraulic and thermal characteristics to undisturbed soil, including changes to soil density, conductivities, and volumetric heat capacity. These changes also depend on whether the soil has been compacted or loosened. There is no discernable effect from disturbance of the sand since it has such low cohesion, but this case is an exception.

Hysteresis was not included for this modeling since the sand possesses a highly uniform, simple soil matrix. Hysteresis is the difference in a change dependent on the

direction of that change (Radcliffe 2010). For soils, it is often the case that the hydraulic conductivity of a wetting soil changes differently than for a drying soil since air pockets can develop in pores while saturating. This causes a dual behavior seen in the SWRC, which should be considered when modeling more complex soils.

Hydrus 1D uses an internal set of equations to determine potential evaporation and the associated latent heat flux. These estimates are not validated for this study, with no alternative method used to estimate latent heat flux. Vapor transport is not incorporated into the models, which can be important especially in water-limited conditions when soil moisture is drawn from deeper in the soil column. With a more complete modeling approach, the shift from surface evaporation (stage 1) to subsurface evaporation (stage 2) is an important factor to consider, as it changes the dynamics of vapor flow through the soil and into the atmosphere (Deol 2012). Hydrus attempts to pinpoint this transition using a value called hCritA, representing the minimum allowed pressure head at the soil surface, or the threshold below which actual evaporation is less than potential evaporation (Šimůnek 2003). hCritA can be determined two ways. The Hydrus manual provides an equation for calculating hCritA (a matric head) from relative humidity, though for course soils this is often too high a value to allow for model convergence (Šimůnek 2005). The alternative is to set hCritA based on soil texture, or as a default setting. This decision may warrant closer investigation for future modeling efforts.

EcoCELL Tests – Experimental Design

Experiments constructed in the DRI EcoCELL laboratory have the benefit of regulated environmental controls used to generate a wide range of temperatures and soil moistures over four long-term environmental simulations. These experiments were

carefully constructed to create realistic conditions encountered when detecting landmines. All available soil sensors were used to optimize the distribution of observed data points surrounding the artificial targets, providing a strong framework from which to construct the Hydrus 2D models. Aside from a few faulty sensors, the physical experiments ran smoothly and without any major breaks in functionality. However, in retrospect and with future experiments in mind, several adjustments to experimental design are recommended.

Arguably the most critical oversight in our experiments was to not monitor the surface temperature of the EcoCELL soil plots directly. An infrared temperature sensor used to measure even a single point temperature for the duration of the tests could serve as a specified thermal UBC for the Hydrus 2D modeling. Scaling the Sensor 1 record (Figure 12) would not be necessary in that case, and that record could be incorporated into model calibration. With the next deepest sensors at 30.5 cm depth (Figure 5), data from the Sensor 1 record is crucial to properly constrain heat flow parameters to match observed data close to the soil surface. The Hydrus 2D heat model did not generate any meaningful results, aside from the Sensor 7 residuals indicating a bias towards the more often saturated sensors, and thus a perceived difference in soil temperatures associated with water content. A higher density of sensors near the surface makes sense given the focus of this research on surface processes. Increasing the number of sensors was not possible for these tests, but they should have been concentrated more towards the surface where thermal variability is more dynamic.

The ideal model to simulate surface temperature associated with subsurface water flow will be supported fully by direct measurements, especially when testing whether the model can accurately match those measurements to then be applied to a wider variety of

conditions. Without a direct comparison the results are one step removed from reality. The more variables that can be measured or fixed experimentally without modeling the better, including meteorological inputs, soil flow parameters, and other factors such as water temperature. To capture the dynamics of water flowing down and around an impermeable object, a model must be able to resolve flow in two dimensions, as with Hydrus 2D. It must also have the functionality to balance energy fluxes at the surface as with Hydrus 1D. For this purpose, further modeling is currently in development at DRI using a COMSOL Multiphysics model, which may solve many of the issues uncovered by this research.

Conclusions and Recommendations

The Hydrus software does not meet the requirements of this study, and several flaws in experimental design must be considered for future research using the EcoCELL test bed. Hydrus 2D does not include a way to estimate surface energy balance, and Hydrus 1D is unable to replicate the observed flow patterns around Target A. Accurately simulating surface heat above a buried object within variably saturated soil requires either a modeled system capable of estimating surface temperatures based on energy balance and capable of resolving spatial flow patterns for water and heat, or it requires an experimental setup that directly measures surface temperature or the meteorological variables needed to calculate surface temperature.

Hypothesis 1 - Negative

HYDRUS 2D cannot be used to generate to simulate surface temperature associated with the flow of water and heat around a buried, impermeable object. However, this research demonstrates the usefulness of Hydrus 2D in constraining Van Genuchten flow

parameters and simulating subsurface water flow. Modeling water flow shows that the presence of Target A alters water flow around the target (Figures 3, 17, 25). Without the ability to model surface temperatures, neither research question posed by this study was answered using Hydrus 2D.

<div align="center">Hypothesis 2 – Mixed Results</div>

HYDRUS 1D modeling can supplement the 2D model to account for the surface energy budget, including latent and radiant heat terms, though its application is limited. Hydrus 1D can simulate surface temperatures based on environmental inputs, and on the thermal properties of Target A and sand, but it is unable to replicate water flow around Target A.

The results of the 1D modeling effort point to the fact that increased soil moisture above a buried object creates a zone of damped temperature response to natural temperature variations, owing to the increased volumetric heat capacity of saturated soil. 1D modeling results also show that the temperature difference associated with saturated versus dry experiments are greater than those with versus without Target A. For these modeled conditions, the relatively higher differences between saturated and dry conditions support the idea that soil watering can be used to improve thermal contrast above a buried object, independent of that objects' material properties.

While this result is promising for further research, this method does not provide the quantitative rigor necessary to support demining operations. Without direct measurements of surface temperature with which to confirm model accuracy, it is impossible to confidently quantify the surface thermal response to water flow in the shallow subsurface.

Recommendations

- If possible, the scope of future modeling efforts should include greater range of soil properties, target materials, target shapes, and target depths.

- It may be prudent to consider the effects of organic matter, surface roughness, soil disturbance, hysteresis, vapor transport, and changes in evaporation dynamics (hCritA). This modeling is a step in understanding the soil processes underlying thermal mine detection, but it does not fully replicate field conditions and is not appropriate for operational use.

- The experimental design of the EcoCELL experiments should be revised for continued similar research. Soil surface temperature and the temperature of incoming water should be monitored, as well as radiation balance if possible. Soil sensors should be concentrated closer to the surface.

- The Hydrus software does not meet the requirements of this study, and a different numerical model is needed to continue this research. Ideally, a model should be able to synthesize the individual benefits of Hydrus 2D and 1D, with the ability to resolve spatial flow patterns around a buried object, and the ability to constrain surface energy fluxes to simulate the resultant changes in surface temperature.

References

1. Abu-Hamdeh, N. H. (2003). Thermal properties of soils as affected by density and water content. Biosystems engineering, 86(1), 97-102.

2. Allen, R. G., Pereira, L. S., Raes, D., & Smith, M. (1998). Guidelines for computing crop water requirements-FAO Irrigation and drainage paper 56, FAO-Food and Agriculture Organization of the United Nations, Rome (http://www. fao. org/docrep) ARPAV (2000), La caratterizzazione climatica della Regione Veneto, Quaderni per. Geophysics, 156, 178.

3. Baytos, J. F. (1979). Specific heat and thermal conductivity of explosives, mixtures, and plastic-bonded explosives determined experimentally (No. LA-8034-MS). Los Alamos Scientific Lab., NM (USA).

4. Boltzmann, L. (1884). Ableitung des Stefan'schen Gesetzes, betreffend die Abhängigkeit der Wärmestrahlung von der Temperatur aus der electromagnetischen Lichttheorie. Annalen der Physik, 258(6), 291-294.

5. Bouwer, H., & Rice, R. C. (1984). Hydraulic Properties of Stony Vadose Zones a. Groundwater, 22(6), 696-705.

6. Brooks, R., & Corey, T. (1964). Hydraulic properties of porous media. Hydrology Papers, Colorado State University, 24, 37.

7. Bruschini, C., & Gros, B. (1997, September). A survey of current sensor technology research for the detection of landmines. In Proc. International Workshop on Sustainable Humanitarian Demining (Vol. 6, pp. 18-27).

8. Caldwell, T.G., McDonald, E.V., Mihevc, T.M., Bacon, S.N. (2012). Monitoring the electrical and thermal properties of disturbed soils for military operations. Unpublished. For submission to the ICMG Conference Proceedings.

9. Carslaw, H. S., & Jaeger, J. C. (1959). Conduction of heat in solids: Oxford Science Publications (p. 510). Oxford, England.

10. Chung, S. O., & Horton, R. (1987). Soil heat and water flow with a partial surface mulch. Water Resources Research, 23(12), 2175-2186.

11. Darcy, H. (1856). Public fountains in the city of Dijon and exhibition purposes. Victor Dalmont.

12. Daniels, D. J. (2009). Ground penetrating radar for buried landmine and IED detection. In Unexploded Ordnance Detection and Mitigation (pp. 89-111). Springer, Dordrecht.

13. Das, B. S., Hendrickx, J. M., & Borchers, B. (2001). Modeling transient water distributions around landmines in bare soils. Soil Science, 166(3), 163-173.

14. De Marsily, G. (1986). Quantitative hydrogeology. Paris School of Mines, Fontainebleau.

15. Decagon Devices (2010). 5TE, water content, EC and temperature sensors: Operator's manual, version 6. Decagon Devices Inc.: Pullman, WA, USA.

16. Deol, P., Heitman, J., Amoozegar, A., Ren, T., & Horton, R. (2012). Quantifying nonisothermal subsurface soil water evaporation. Water Resources Research, 48(11).

17. Derzko, Z., Nguyen, O., Phan, C., Lydic, R., & Broach, T. (2012). Rain effects on physical soil temperatures with buried targets. Detection and Sensing of Mines, Explosive Objects, and Obscured Targets XVII. In Proc. of SPIE Vol 8357.

18. DeVries, D. A. (1963). Thermal properties of soils. In 'Physics of plant environment'(Ed. WR van Wijk) pp. 210–235.

19. Dingman, S. L. (2015). Physical hydrology. Waveland press.

20. Donskoy, D., Ekimov, A., Sedunov, N., & Tsionskiy, M. (2002). Nonlinear seismo-acoustic land mine detection and discrimination. The Journal of the Acoustical Society of America, 111(6), 2705-2714.

21. Duffield, G. (2019, June 06). Aquifer testing 101: Hydraulic properties representative values of hydraulic properties. Retrieved from http://www.aqtesolv.com/aquifer-tests/aquifer_properties.htm

22. Elger, D. F., Williams, B. C., Crowe, C. T., & Roberson, J. A. (2009). Engineering fluid mechanics. Energy, 2, 03-01.

23. Engineeringtoolbox.com. (2019). Engineering Toolbox. [online] Available at: http://www.engineeringtoolbox.com/ [Accessed December 2018].

24. Fetter, C. W. (2001). Applied Hydrogeology (4 th). Supplemental website http://www. appliedhydrogeology. info. Upper Saddle River, NJ: Prentice Hall, 598.

25. Fourier, J. (1822). Analytical Theory of Heat, by M. Fourier . At Firmin Didot, father and son.

26. Furbish, D. J. (1996). Fluid physics in geology: An introduction to fluid motions on Earth's surface and within its crust. Oxford University Press.

27. Garcia-Padron, R., Loyd, D., & Sjökvist, S. (2002). Heat and moisture transfer in wet sand exposed to solar radiation—Models and experiments concerning buried objects. Subsurface Sensing Technologies and Applications, 3(2), 125-150.

28. Hargreaves, G. H. (1994). Defining and using reference evapotranspiration. Journal of Irrigation and Drainage Engineering, 120(6), 1132-1139.

29. Hargreaves, G. H., & Samani, Z. A. (1982). Estimating potential evapotranspiration. Journal of the Irrigation and Drainage Division, 108(3), 225-230.

30. Hazen, A. (1893). Some physical properties of sand and gravels. Massachusetts State Board of Health. 24th Annual Report.

31. Hong, S. H., Miller, T. W., Tobin, H., Borchers, B., Hendrickx, J. M., Lensen, H. A., ... & Baertlein, B. A. (2001, October). Impact of soil water content on landmine detection using radar and thermal infrared sensors. In Detection and Remediation Technologies for Mines and Minelike Targets VI (Vol. 4394, pp. 409-417). International Society for Optics and Photonics.

32. Jensen, Marvin E., and Richard G. Allen, eds. "Evaporation, evapotranspiration, and irrigation water requirements." American Society of Civil Engineers, 2016.

33. Jensen, D. T., Hargreaves, G. H., Temesgen, B., & Allen, R. G. (1997). Computation of ETo under nonideal conditions. Journal of Irrigation and Drainage Engineering, 123(5), 394-400.

34. Joule, J. P. (1884). Scientific Papers, Vol. 1. London, 322, 1843.

35. Jurin, J. (1718). An account of some experiments relating to the specific gravity of human blood. Phil Trans Roy Soc London, 30, 1000-14.

36. Karlsson, E., & Pomade, L. (2013). Methods of estimating potential and actual evaporation. Salt Lake City: Department of Water Resources Engineering.

37. Kersten, M. S. (1949). Laboratory Research for the Determination of the Thermal Properties of Soils. Minnesota univ Minneapolis engineering experiment station.

38. Kirkham, D., & Powers, W. L. (1972). Advanced soil physics (No. BOOK). Wiley.

39. Landmine Monitor 2016 (Rep.). (2016). Intl. Campaign to Ban Landmines - Cluster Munition Coalition.

40. Law, A. D. S. (2004) Saturated Hydraulic Conductivity: Water Movement Concepts and Class History.

41. Leij, F. J., Skaggs, T. H., & Van Genuchten, M. T. (1991). Analytical solutions for solute transport in three-dimensional semi-infinite porous media. Water resources research, 27(10), 2719-2733.

42. Lide, D. R. (Ed.). (2004). CRC handbook of chemistry and physics (Vol. 85). CRC press.

43. McDonald, E., Caldwell, T., Mihevc, T., Baker, S., Bacon, S., Jenkins, S., ... & Schumer, R. (2013). Global Military Operating Environments (GMOE) Phase I: Linking Natural Environments, International Security, and Military Operations. DESERT RESEARCH INST RENO NV.

44. McDonald, E.V., Sabol, D., Hausner, M. (2015). Soil Characterization of Lane 49 CAL at Countermine Facility: Methods, Data, and Results Report.

45. Mualem, Y. (1976). A new model for predicting the hydraulic conductivity of unsaturated porous media. Water resources research, 12(3), 513-522.

46. Penman, H. L. (1948). Natural evaporation from open water, bare soil and grass. Proc. R. Soc. Lond. A, 193(1032), 120-145.

47. Priestley, C. H. B., & Taylor, R. J. (1972). On the assessment of surface heat flux and evaporation using large-scale parameters. Monthly weather review, 100(2), 81-92.

48. Quikrete Companies, LLC. (2018). Commercial Grade Sands: Product Numbers 1961, 1962, 1963. Retrieved March 2020, from https://www.quikrete.com/pdfs/data_sheet-commercial grade sands.pdf

49. Radcliffe, D. E., & Šimůnek, J. (2010). Soil physics with HYDRUS: Modeling and applications. Boca Raton, FL: CRC Press/Taylor & Francis.

50. Richards, L. A. (1931). Capillary conduction of liquids through porous mediums. physics, 1(5), 318-333.

51. Robinson, D. A., Gardner, C. M. K., & Cooper, J. D. (1999). Measurement of relative permittivity in sandy soils using TDR, capacitance and theta probes: comparison, including the effects of bulk soil electrical conductivity. Journal of Hydrology, 223(3-4), 198-211.

52. Saito, H., Šimůnek, J., & Mohanty, B. P. (2006). Numerical analysis of coupled water, vapor, and heat transport in the vadose zone. Vadose Zone Journal, 5(2), 784-800.

53. Schaetzl, R. J., & Thompson, M. L. (2015). Soils. Cambridge university press.

54. Shati, A. K. A., Blakey, S. G., & Beck, S. B. M. (2011). The effect of surface roughness and emissivity on radiator output. Energy and Buildings, 43(2-3), 400-406.

55. She, H. Y., & Sleep, B. E. (1998). The effect of temperature on capillary pressure-saturation relationships for air-water and perchloroethylene-water systems. Water Resources Research, 34(10), 2587-2597.

56. Šimůnek, J. (2017). Re: HeatTransport BC. Retrieved from https://www.pc-progress.com/forum/

57. Šimůnek, J., Van Genuchten, M. T., & Šejna, M. (2016). Recent developments and applications of the HYDRUS computer software packages. Vadose Zone Journal, 15(7).

58. Šimůnek, J., M. Šejna, H. Saito, M. Sakai, and M. Th. van Genuchten (2008). The HYDRUS-1D software package for simulating the one-dimensional movement of water, heat, and multiple solutes in variably-saturated media, Version 4.0, Hydrus Series 3, Department of Environmental Sciences, University of California Riverside, Riverside, CA, USA. *Internal Hydrus 1D Help Files.*

59. Šimůnek, J. (2006). Re: heat transport. Retrieved from https://www.pc-progress.com/forum/

60. Šimůnek, J., Van Genuchten, M. T., & Šejna, M. (2006). The HYDRUS software package for simulating two-and three-dimensional movement of water, heat, and multiple solutes in variably-saturated media. Technical manual, version, 1, 241.

61. Šimůnek, J., Van Genuchten, M. T., & Sejna, M. (2005). The HYDRUS-1D software package for simulating the one-dimensional movement of water, heat, and multiple solutes in variably-saturated media. University of California-Riverside Research Reports, 3, 1-240.

62. Šimůnek, J. (2003). Re: hCritA value. Retrieved from https://www.pc-progress.com/forum/

63. Šimůnek, J., Hendrickx, J. M., & Borchers, B. (2001, October). Modeling transient temperature distributions around landmines in homogenous bare soils. In Detection and Remediation Technologies for Mines and Minelike Targets VI (Vol. 4394, pp. 387-398). International Society for Optics and Photonics.

64. Smits, K. M., Cihan, A., Sakaki, T., Howington, S. E., Peters, J. F., & Illangasekare, T. H. (2013). Soil moisture and thermal behavior in the vicinity of buried objects affecting remote sensing detection: Experimental and modeling investigation. IEEE Transactions on Geoscience and Remote Sensing, 51(5), 2675-2688.

65. Smits, K. M., Sakaki, T., Limsuwat, A., & Illangasekare, T. H. (2010). Thermal conductivity of sands under varying moisture and porosity in drainage–wetting cycles. Vadose Zone Journal, 9(1), 172-180.

66. Sophocleous, M. (1979). Analysis of water and heat flow in unsaturated-saturated porous media. Water Resources Research, 15(5), 1195-1206.

67. Stallman, R. W. (1965). Steady one-dimensional fluid flow in a semi-infinite porous medium with sinusoidal surface temperature. Journal of geophysical Research, 70(12), 2821-2827.

68. Turc, L. (1961). Estimation of irrigation water requirements, potential evapotranspiration: a simple climatic formula evolved up to date. Ann. Agron, vol. 12, no. 1, pp. 13-49.

69. UMS (2015): Manual HYPROP, Version 2015-01, 96 pp. UMS GmbH, Gmunder Straße 37, Munich, Germany. URL http://ums-muc.de/static/Manual_HYPROP.pdf

70. Van Bavel, C. H. M., & Hillel, D. I. (1976). Calculating potential and actual evaporation from a bare soil surface by simulation of concurrent flow of water and heat. Agricultural Meteorology, 17(6), 453-476.

71. Van Dam*, R. L., Borchers, B., & Hendrickx, J. M. (2005). Strength of landmine signatures under different soil conditions: implications for sensor fusion. International Journal of Systems Science, 36(9), 573-588.

72. Van Dam, R. L., Borchers, B., Hendrickx, J. M., & Hong, S. H. (2003, September). Soil effects on thermal signatures of buried nonmetallic landmines. In Detection and Remediation Technologies for Mines and Minelike Targets VIII (Vol. 5089, pp. 1210-1219). International Society for Optics and Photonics.

73. Van Genuchten, M. T., & Parker, J. C. (1984). Boundary conditions for displacement experiments through short laboratory soil columns 1. Soil Science Society of America Journal, 48(4), 703-708.

74. Viessman, W., Lewis, G. (2003), Introduction to Hydrology. Fifth Edition. New York, New York.

75. Wijk, W. V. (1963). Physics of plant environment. John Wiley & Sons.

76. Xu, C. Y., & Singh, V. P. (2000). Evaluation and generalization of radiation-based methods for calculating evaporation. Hydrological processes, 14(2), 339-349.